Measurement report: Impacts of Thermodynamic and Dynamic Processes on the Vertical Distribution of Carbonaceous Aerosols: lessons from in-situ observations at eastern foothills of Liu~~P~~pan Mountains, Loess Plateau

Shaofeng Qi[1, 2], Suping Zhao [1, 3*], Ye Yu[1, 3], Longxiang Dong[1, 3], Tong Zhang[1, 3], Guo Zhao[1, 2, 3], Jianglin Li[1, 3], Xiang Zhang[1, 2], Yiting Lv[1, 2]

1. Key Laboratory of Cryospheric Science and Frozen Soil Engineering, Northwest Institute of Eco-Environment and Resources, Chinese Academy of Sciences, Lanzhou 730000, China.
2. University of Chinese Academy of Sciences, Beijing 100049, China.
3. Pingliang Land Surface Process & Severe Weather Research Station, Pingliang 744015, China.

Correspondence to: Suping Zhao (zhaosp@lzb.ac.cn)

Abstract. The vertical distribution of carbonaceous aerosols critically influences planetary boundary layer structure and regional climate~~climate impacts~~. However, high-resolution vertical data remain scarce over the Chinese Loess Plateau. To address this gap, coordinated observations of carbonaceous aerosols and meteorological variables were conducted in the Loess Plateau using tethered balloon-borne instruments during two field campaigns in July 2023 and 2024. The average near-surface concentrations of equivalent black carbon (eBC) and ultraviolet-absorbing particulate matter (UVPM) in Pingliang were ~~0.82~~0.84 μg m^{-3} and ~~1.26~~1.24 μg m^{-3}, respectively. Vertically, carbonaceous aerosol concentrations generally decreased with height. A comparison of the vertical profiles of eBC, UVPM, V_{TKE}~~VTKE~~ (mechanical turbulence), and potential temperature showed that during the early morning and nighttime, when convective activity was weak, UVPM concentrations in the upper atmosphere were higher than those of eBC. This pattern is primarily

attributed to nucleation processes involving gaseous precursors during nighttime. Analysis of the roles of dynamic and thermodynamic processes indicated that thermodynamic processes dominated aerosol vertical transport in the near-surface layer, while enhanced dynamic processes at higher altitudes facilitated horizontal dispersion of pollutants. Air masses from the south of the observation site contributed significantly to UVPM levels. As air mass altitude decreased, the influence of local sources became more pronounced. Overall, this study demonstrated the regulatory mechanism of daytime and nighttime thermodynamic and dynamic impacts on the vertical distribution of air pollutants.

1. Introduction

Carbonaceous aerosols, particulate matter generated from fossil fuel combustion and biomass burning, directly impact the Earth-atmosphere energy budget by absorbing solar radiation. Their primary components are organic carbon (OC) and black carbon (BC). Organic carbon (OC) can be broadly classified into primary organic carbon (POC) and secondary organic carbon (SOC). The primary organic carbon originates directly from sources such as biomass burning, vehicle exhaust, and industrial emissions, whereas SOC is formed through the oxidation of volatile organic compounds (VOCs) via photochemical and dark reaction pathways. Due to its complex chemical composition and the strong ultraviolet light absorption of certain organic fractions, which are referred to as brown carbon (BrC), OC introduces substantial uncertainty into climate impact assessments (Kroll et al., 2011).~~OC encompasses both primary organic carbon (POC) emitted directly from biomass burning and secondary organic carbon (SOC) formed through the photochemical reactions of volatile organic compounds (VOCs). Due to its complex chemical composition, OC introduces substantial uncertainty in climate effect assessments (Kroll et al., 2011).~~ Black carbon ~~(BC)~~, characterized by strong solar radiation absorption, represents the second-largest anthropogenic climate ~~forcer~~factor after CO_2 (Bond et al., 2013; Ramanathan & Carmichael, 2008). Near the base of the

stratosphere, BC's direct radiative forcing can be approximately ten times stronger than at the surface (Samset & Myhre, 2011). Consequently, its vertical position within the atmosphere significantly influences atmospheric stratification (Zhang et al., 2017; Zhao et al., 2021). Within the surface layer, BC can heat the lower atmosphere, enhancing convection and promoting planetary boundary layer (PBL) development. At higher altitudes, however, BC heats the atmosphere while simultaneously reducing solar radiation reaching the surface, leading to increased atmospheric stability. This suppresses ~~boundary layer~~the PBL development and exacerbates air pollution (Ding et al., 2016; Petäjä et al., 2016; Wang et al., 2018a).

Over complex terrain, valley wind systems and orographically-induced turbulence can transport surface-emitted BC to higher elevations, where it accumulates within temperature inversion layers. Absorptive BC further heats the atmosphere, suppressing the development of the PBL~~planetary boundary layer (PBL)~~ and altering its height and stability (Zhao et al., 2023a). Additionally, BC modifies cloud microphysical properties, influencing cloud formation, dissipation, and precipitation, thereby affecting regional and global climate systems (Panicker et al., 2014; Wendisch et al., 2008). Over recent decades, the radiative forcing and climate effects of BC have been extensively studied. Published estimates of BC's direct radiative forcing range between 0.25 – 0.90 W m^{-2} (Allen & Landuyt, 2014), yet these values are subject to considerable uncertainty. A primary source of this uncertainty is the significant spatiotemporal heterogeneity of BC at the global scale, stemming from regional combustion processes and its short atmospheric lifetime. Consequently, using default model BC profiles to simulate radiative forcing introduces substantial errors (Hodnebrog et al., 2014). Reported studies indicate that differences in BC vertical distribution contribute approximately 20 – 40% to the uncertainty in calculations of BC's top-of-atmosphere radiative forcing (Chen et al., 2022; Zarzycki & Bond, 2010). Therefore, accurately characterizing the true vertical distribution of BC in the atmosphere is crucial for the precise assessment of its regional and global climate effects.

However, acquiring accurate BC vertical profiles remains a significant challenge for researchers globally. Current observation methods include: Tethered balloons (Guan et al., 2022; Lata et al., 2023; Wang et al., 2021a; Zhao et al., 2023a), Aircraft measurements (Moorthy et al., 2004; Schwarz et al., 2017), Unmanned Aerial Vehicles (UAVs) (Liu et al., 2020; Wang et al., 2021b; Wu et al., 2021), Cable cars (Zawadzka et al., 2017), Meteorological towers (Wang et al., 2018b; Xie et al., 2019), Topography-dependent in-situ observations (Zhao et al., 2019; 2022). Notably, aircraft measurements face operational constraints in complex terrain due to high costs and requirements for expansive landing areas. UAVs, cable cars, and meteorological towers are limited by maximum achievable altitudes – most UAVs typically reach only ~500 m, while cable cars and towers cover even lower vertical ranges. Though topography-dependent observations are widely applied in complex terrain, their coarse spatial resolution cannot resolve true vertical distributions of atmospheric constituents. Additionally, while lidar remote sensing enables continuous profiling (Miffre et al., 2015), its accuracy remains inferior to in-situ techniques. In contrast, tethered-balloon systems mitigate these key constraints by providing high-resolution BC profiles within the ~~planetary boundary layer~~PBL. This approach has been widely applied in various regions across the globe, including Europe, the Arctic, the United States, and South Asia, as well as several key regions in China, such as the North China Plain, the Sichuan Basin, and the Yangtze River Delta~~This approach has been successfully deployed across diverse regions including Europe, the Arctic, South Asia, and China's North China Plain, Sichuan Basin, and Yangtze River Delta~~ (Bisht et al., 2016; Mazzola et al., 2016; Guagenti et al., 2025; Ran et al., 2016; Samad et al., 2020; Wang et al., 2018b; Zhao et al., 2023a).

Pingliang City, situated in eastern Gansu Province, lies at the convergence of Shaanxi, Gansu, and Ningxia provinces. As a significant component of the Loess Plateau and a major agricultural zone in Northwest China, understanding its climatic-environmental mechanisms is crucial for improving meteorological forecasting accuracy and

formulating effective pollution control strategies. The region's complex topography facilitates the transport of urban pollutants to higher-elevation loess tablelands via valley wind circulations, enabling dispersion during transit. Furthermore, influenced by the towering Liupan Mountains, Pingliang exhibits pronounced vertical climatic heterogeneity, resulting in intricate feedback mechanisms between the ~~planetary boundary layer~~ PBL and aerosols. Current research reveals scarce data on the vertical distribution of BC from fossil fuel combustion, biomass burning, and mineral dust activities in this region. To address this gap, we conducted detailed vertical profile observations using tethered balloon-borne instrumentation over typical loess tableland areas during July 2023 and July 2024. This study aims to supplement the deficiency in local BC aerosol observations, establish a database for assessing aerosol climate effects on the Loess Plateau, and ultimately provide scientific foundations for pollution control strategies.

2. Materials and methods

2.1 Observation methods and data sources

Field observations were conducted at the Pingliang Land Surface Processes and Severe Weather Research Station ~~(Pingliang Station)~~, Chinese Academy of Sciences, during two intensive campaigns from 15 to 24 July 2023 and 17 to 30 July 2024. The station is located in Baimiao Township, Pingliang City, Gansu, with geographic coordinates detailed in Figure 1. The near-surface meteorological parameters and air pollutant concentrations for Pingliang City are displayed in Figure S1. This includes the concentrations of PM_{10}, $PM_{2.5}$, CO, SO_2, NO_2, and O_3 during the study periods. ~~Near-surface meteorological parameters at Pingliang Station and the Air Quality Index (AQI) for Pingliang City during the observation periods are presented in Figure S1, while Figure S2 displays concentrations of PM_{10}, $PM_{2.5}$, CO, SO_2, NO_2, and O_3 in Pingliang's urban area.~~ Meteorological data were obtained from near-surface observations at ~~Pingliang~~ the ~~S~~station, and air quality measurements originated from the Pingliang Environmental Monitoring Station (Station ID: 2656A; http://eia-

data.com/). Results indicate that southeasterly or northwesterly winds prevailed ~~at Pingliang Station~~ during the observation periods, with wind speeds typically below 1 m s^{-1}. The mean temperature was 20.76°C and mean relative humidity was 76.84%. Air quality in Pingliang remained generally good except during sporadic dust pollution events.

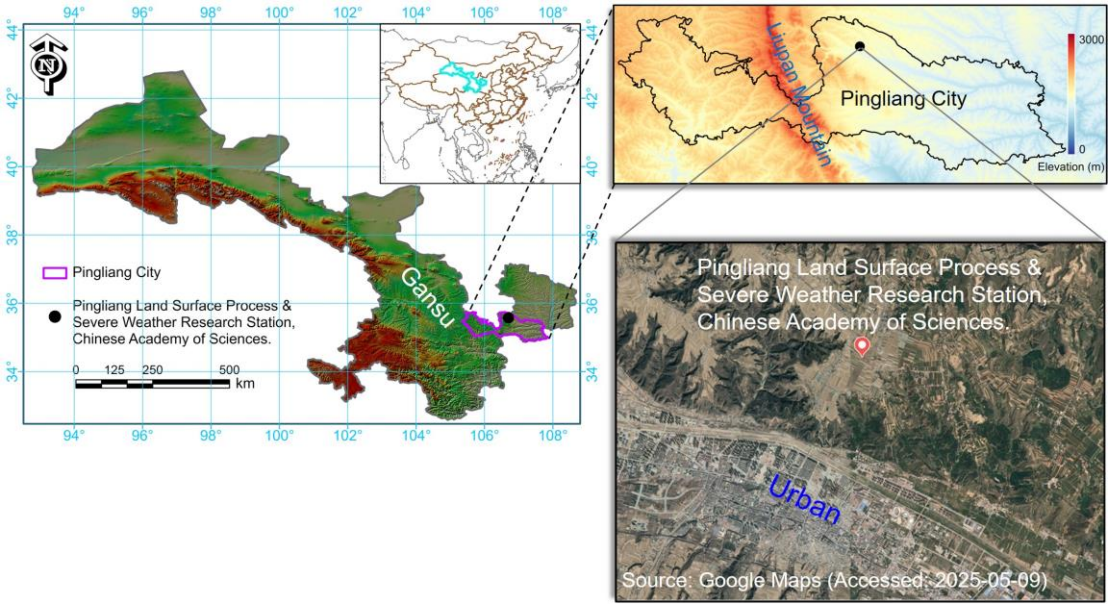

Figure 1. Geographic location of the observation site. The map is a pure reproduction of Google Maps with added marks for our study locations. Copyright © Google Maps. Publisher's note: Please note that the above figure contains disputed territories.

2.1.1 Tethered balloon platform

Vertical profiling was primarily conducted using instrumentation suspended from a tethered balloon system. The system comprised a 10 m^3 helium-filled balloon, a tether line, and an electrically powered winch that actively regulated both ascent and descent rates. Buoyancy provided initial lift, while the winch precisely controlled vertical maneuvering. Instruments were mounted 30 m below the balloon to minimize direct atmospheric disturbance. A MicroAeth® MA350 aerosol monitor measured vertical distributions of carbonaceous aerosols, and an iMet-4 radiosonde (iMet, USA) acquired temperature and humidity profiles. Observations were conducted at 3-hour intervals from 05:00 to 23:00 ~~local time~~LT (05:00, 08:00, 11:00, 14:00, 17:00, 20:00, 23:00 LT) daily. Operations were suspended during adverse conditions (e.g., strong

winds or precipitation). Complementary vertical wind profiles were obtained using Doppler Beam Steering (DBS) mode of a Leosphere Windcube 200s lidar. Each balloon sounding lasted approximately 30 – 60 minutes, during which atmospheric conditions remained relatively stable, allowing both ascent and descent paths to characterize vertical structures. A total of 24 and 39 soundings were completed during summer 2023 and 2024 respectively (Figure S2 shows the observation frequency by time period), yielding 126 vertical atmospheric profiles.

2.1.2 Carbonaceous aerosol mass concentrations

The MicroAeth® MA350 determines ~~BC~~carbonaceous aerosols concentration based on the Beer-Lambert law, quantifying light absorption by carbonaceous particles deposited on a PTFE filter at multiple wavelengths. The instrument employs five laser wavelengths: 375 nm (UV), 470 nm (Blue), 528 nm (Green), 625 nm (Red), and 880 nm (IR). Carbon concentrations measured at 880 nm are considered to represent the equivalent black carbon concentration (denoted as eBC) (Zhao et al., 2023a), whereas those measured at 375 nm correspond to ultraviolet-absorbing particulate matter (UVPM), which includes primary brown carbon and black carbon emitted from sources such as biomass burning and coal combustion, as well as secondary brown carbon formed through atmospheric oxidation processes (The relevant introduction/details regarding the substance measured at a wavelength of 375 nm can be referenced in the official manual of the MicroAeth® MA Series MA300 instrument. URL: https://aethlabs.com/products/ma300, last accessed: 13 November 2025). ~~Carbon concentration measured at 880 nm is considered equivalent to BC concentration (denoted as IRBC or BC) (Zhao et al., 2023), while measurements at 375 nm represent Ultraviolet Particulate Matter (UVPM) associated with biomass combustion (e.g., wood, straw).~~ The Absorption Ångström ~~Absorption~~ Exponent (AAE), calculated from multi-wavelength measurements, characterizes the wavelength dependence of carbonaceous aerosol absorption. During this study, the MA350 operated at a flow rate of 150 mL min^{-1} with a 5-second sampling interval. Negative optical attenuation (ATN) values occasionally occurred under low aerosol

concentrations at high altitudes, which were corrected using the Optimized Noise-reduction Averaging (ONA) algorithm (Hagler et al., 2011; Guan et al., 2022).

2.2 Calculation of light absorption coefficient for carbonaceous aerosols

The light absorption coefficient (b_{Abs}) of black carbon was calculated using the following Eq. (1):

$$b_{Abs} = MAC_{BC}(\lambda) \times [BC] \quad (1),$$

where $MAC_{BC}(\lambda)$ denotes the mass absorption cross-section of carbonaceous aerosols at specific wavelengths. For the MicroAeth® series instruments, the MAC values at 375 nm, 470 nm, 528 nm, 625 nm, and 880 nm are 24.07 $m^2\ g^{-1}$, 19.07 $m^2\ g^{-1}$, 17.03 $m^2\ g^{-1}$, 14.09 $m^2\ g^{-1}$, and 10.12 $m^2\ g^{-1}$, respectively (Zhao et al., 2023a). The [BC] represents the concentration of carbonaceous aerosol at different wavelengths.

Additionally, the light absorption coefficient of carbonaceous aerosols can be expressed as:

$$b_{Abs}(\lambda) = k \times \lambda^{-AAE} \quad (2).$$

In Eq. (2), k is a wavelength-independent constant, and AAE represents the Ångström Absorption Ångström Exponent, which characterizes the wavelength dependence of light absorption of carbonaceous aerosols (Ångström, 1929). A higher AAE value signifies that the aerosol absorption capacity decreases more rapidly with increasing wavelength. By combining the b_{Abs} values derived from Eq. (1) with Eq. (2), vertical profiles of AAE for carbonaceous aerosols were obtained.

2.3 Determination of planetary boundary layer height

Potential temperature (θ, in K), defined as the temperature an air parcel would attain if adiabatically brought to a standard pressure level (Han et al., 2019; Seidel et al., 2010), is calculated as Eq. (3):

$$\theta = (T+273.15) \times \left(\frac{P_0}{P}\right)^{\frac{R_d}{C_{pd}}} \quad (3)$$

where T denotes measured air temperature (°C), P represents air pressure (hPa), P_0 is the standard reference pressure (1000 hPa), R_d signifies the gas constant for dry air (287 J kg^{-1} K^{-1}), and C_{pd} corresponds to the specific heat of dry air at constant pressure (1005 J kg^{-1} K^{-1}) (Gu et al., 2025).

Specific humidity (q, g g^{-1}), defined as the ratio of water vapor mass to the total mass of moist air (water vapor plus dry air), is calculated using Eq. (4) (Gutzler, 1992),

$$q = \frac{\varepsilon \times e}{P - 0.378 \times e} \quad (4)$$

where $\varepsilon = 0.622$, e represents vapor pressure, and P denotes atmospheric pressure, with vapor pressure, e being derived from Eq. (5) through relative humidity (RH) and air temperature (T, °C) (Holzworth, 1964).

$$e = 6.105 \times RH \times \exp\left(\frac{17.7 \times T}{237.7+T}\right) \quad (5).$$

Planetary boundary layer is the part of the atmosphere closest to the planet's surface, accounting for approximately 10% – 20% of the troposphere. It is the lowest layer of the troposphere directly influenced by surface forcing, with a response time of less than one hour, playing a critical role in the dispersion and transport of air pollutants. Within the PBL, turbulent mixing processes homogenize air temperature and humidity, resulting in relatively uniform distributions of these properties. PBL height (PBLH) refers to the thickness of the layer most significantly affected by the surface. In other words, it is the vertical extent that surface turbulent motion (caused by surface heating, friction, or topography, etc.) can effectively influence (Emeis et al., 2008; Seibert et al., 2000). This study employs two established methodologies for determining the PBLH: the potential temperature gradient method and the parcel method (Holzworth, 1964; Zhang et al., 2020). The potential temperature gradient method was utilized for calculating the PBLH during the nighttime and early morning hours (20:00, 23:00, 05:00, and 08:00 LT), while the parcel method was applied specifically for the daytime periods (11:00, 14:00, and 17:00 LT). Detailed

computational procedures for both approaches are summarized in Supplementary Table S1.~~The planetary boundary layer (PBL) refers to the lower troposphere directly influenced by surface forcing with a response time of less than one hour, playing a critical role in the dispersion and transport of air pollutants. Within the PBL, turbulent mixing processes homogenize air temperature and humidity, resulting in relatively uniform distributions of these properties. Distinct discontinuities in temperature, humidity, and wind speed typically mark the PBL top (Emeis et al., 2008; Seibert et al., 2000). While various methodologies exist for determining PBL height (PBLH), this study employs two established approaches: the potential temperature gradient method and the parcel method, with detailed computational procedures provided in Supplementary Table S1 (Zhang et al., 2020)~~

2.4 Impacts of thermodynamic and dynamic processes on vertical distribution of carbonaceous aerosols

To quantify the relative contributions of potential temperature gradient, mechanical turbulence index, horizontal wind speed, and vertical wind speed to UVPM variations at different altitudes, we employed a random forest regression algorithm. The model generated training subsets via bootstrap sampling, with random feature subsets selected for optimal splitting at each decision tree node. Observations were categorized into daytime (08:00, 11:00, 14:00, 17:00 LT) and nighttime (20:00, 23:00, 05:00 LT) periods to compare the dominant mechanisms governing aerosol vertical distribution. The mechanical turbulence index was calculated using Eq. (6) (Zhao et al., 2023a).

$$V_{TKE} = 0.5 \times \sqrt{\overline{u}^2 + \overline{v}^2 + \overline{w}^2} \quad (6).$$

2.5 Identification of potential source regions

In this study, GDAS1 meteorological data (1° × 1° resolution) obtained from the NOAA FTP repository (ftp://arlftp.arlhq.noaa.gov/pub/archives/gdas1) were utilized.

These data were processed using the MeteoInfo software to calculate backward trajectories and perform cluster analysis (http://www.meteothink.org/). Subsequently, the potential source contribution function (PSCF) and concentration weighted trajectory (CWT) analysis toolkits within MeteoInfo were employed to identify potential source regions and quantify their relative contributions (Wang, 2014). To reduce the error caused by the small total number of trajectory samples, a weighting factor W_{ij} was introduced, and the weighted PSCF (WPSCF) and weighted CWT (WCWT) were finally calculated. The detailed calculation processes for WPSCF and WCWT are provided in Text 1 of the supplementary material.

3. Results and discussions

3.1 Vertical profiles of carbonaceous aerosols

3.1.1 General characteristics of eBC

Observations indicate that near-surface mass concentrations of eBC and UVPM averaged ~~0.82~~0.84 μg m^{-3} and ~~1.26~~ 1.24 μg m^{-3}, respectively. During the campaign, UVPM concentrations varied between ~~0.21~~0.05 and ~~5.63~~6.78 μg m^{-3} across different altitudes, whereas eBC ranged from ~~0.13~~0.02 to ~~2.05~~2.89 μg m^{-3}. Compared with previous studies conducted in other regions of China (Table 1), the concentration of eBC observed in Pingliang is lower than those reported in Beijing, Shanghai, Nanjing, Chengdu, Shenzhen, Hengshui, the Beibu Gulf region, and Lanzhou (Guan et al., 2022; Ran et al., 2016; Shi et al., 2021; Wang et al., 2021a; Wu et al., 2021; Yang et al., 2023; Yang et al., 2022; Zhao et al., 2023a). This discrepancy can be attributed to several factors. Firstly, Pingliang is a relatively small city with a permanent population of fewer than 2 million, whereas the aforementioned cities have much larger urban populations. Consequently, the total amount of air pollutants generated from daily human activities in Pingliang may be comparatively lower than those in the aforementioned cities.~~Consequently, the total amount of air pollutants generated from daily human activities in Pingliang is comparatively lower.~~ Secondly, the observation site in Pingliang is situated at a higher elevation than the urban center, thereby

reducing the influence of direct urban emissions. In contrast, observation sites in other cities are typically located in suburban areas that are more directly affected by emissions from urban cores.

Wang et al. (2019) conducted tethered-balloon measurements of the vertical distribution of eBC over the Tibetan Plateau and found even lower eBC concentrations than those in the present study. Furthermore, the rate of decrease in eBC concentrations with altitude was more pronounced at the Plateau site compared to Pingliang. Overall, existing studies consistently indicate that eBC concentrations decrease with increasing altitude. However, due to differences in terrain, PBLH, and atmospheric diffusion conditions, the vertical profiles of eBC vary significantly among different sites. For instance, in Shanghai, Wang et al. (2021a) reported a sharp decline in eBC concentrations at around 600 m in the morning, while in the afternoon, the decrease occurred at approximately 800 m due to stronger convective mixing. Over the Tibetan Plateau, eBC concentrations dropped markedly at altitudes as low as 100 – 200 m (Wang et al., 2019). Yang et al. (2023) and Zhao et al. (2023a) reported elevated eBC concentrations near 2000 – 2500 m, which they attributed to the combined effects of upper-level subsidence and lower-level updrafts. Similarly, Lu et al. (2019) and Chen et al. (2022) observed elevated eBC concentrations in the 500 – 800 m layer over Anhui and Beijing, respectively, primarily influenced by the presence of upper-level temperature inversions.

Table 1 Statistics of near-surface eBC concentrations in many cities.

City (Research region)	eBC concentrations (μg m^{-3})	References
Pingliang	0.8 (average)	This study
Beijing	2.0 ~ 6.0	Yang et al., 2022
Shanghai	6.0 ~ 10.5	Wang et al., 2021a
Nanjing	3.2 (average)	Shi et al., 2021
Chengdu	5.0 ~ 8.0	Zhao et al., 2023a
Shenzhen	1.8 ~ 2.5	Wu et al., 2021
Hengshui	5.2 (average)	Ran et al., 2016
Beibu Gulf region	2.3 ~ 4.0	Yang et al., 2023

Lanzhou	3.0 ~ 6.0	Guan et al., 2022

From the global perspectives, the near-surface eBC concentration in Delhi, India, was reported to be approximately 30.00 μg m^{-3}, which is substantially higher than those observed in China and Europe (Bisht et al., 2016). In contrast, near-surface eBC concentrations in Stuttgart, Germany, and Milan, Italy, were found to be comparable to those in Shenzhen, China, at around 2.00 – 3.00 μg m^{-3}. These values are lower than those reported in other Chinese cities such as Shanghai, Nanjing, Chengdu, Hengshui, and Lanzhou, but still higher than the concentrations observed in this study (Ferrero et al., 2011; Samad et al., 2020). In the Arctic region, due to limited anthropogenic influence, near-surface eBC concentrations are generally lower than those observed both over the Tibetan Plateau in China and in the Loess Plateau region investigated in this study (Ferrero et al., 2016).

3.1.2 Diurnal variations of eBC and UVPM profiles

Figures S3 and S4 respectively depict the trends and correlations of the ascent and descent profiles for eBC and UVPM. The results indicate that the ascent and descent profiles at 5:00, 20:00, and 23:00 in this study exhibit similar trends, and thus they can both be treated as independent observational profiles for analysis. For observations at 8:00, 11:00, 14:00 and 17:00, only the ascent data were used for analysis.~~Figures S3 and S4 respectively depict the trends and correlations of the ascent and descent profiles for BC and UVPM. The results indicate that ascent and descent profiles in this study exhibit very similar trends with only minor differences, warranting their combination into a single mean profile.~~ Figure 2 shows the averaged profiles for all sampling periods during the observation campaign, ~~including both ascent and descent legs of the tethered balloon. In Figure 2,~~ the red solid line and its shaded envelope denote the mean and standard deviation~~error~~ of ~~IR~~eBC, while the blue solid line and its shaded envelope denote the mean and standard deviation~~error~~ of UVPM. Because eBC mass concentration in the upper atmosphere is extremely low (below the instrument's normal limit of detection), optical measurements often yield

negative results, which are corrected when the ONA method is used for data quality control. Furthermore, owing to the relatively high wind speeds in the upper atmosphere, our measurements in the early afternoon were typically unable to reach the PBLH.~~daytime measurements in this study generally did not reach the top of the PBL.~~

Vertical profiles of eBC and UVPM concentrations reveal a consistent decrease with increasing altitude, with the most pronounced gradient observed in the near-surface layer. A comparative analysis of their vertical profiles reveals that during periods of weak convective activity, such as early morning and nighttime (i.e., 05:00, 20:00, and 23:00 LT), UVPM concentrations aloft generally exceed those of eBC (the significance test of the UVPM–eBC differences is provided in Figure S5), while near the surface the two species show much smaller differences. To further investigate the underlying causes, we estimated the concentration of secondary UVPM ($UVPM_{sec}$) using the least-squares method described by Wu et al. (2016), based on the ratio of UVPM to eBC. Figure 3 presents the mean diurnal variations in vertical distributions of the ratios of $UVPM_{sec}$ to total UVPM, and of $UVPM_{sec}$ to eBC. From 17:00 to 05:00 LT, the $UVPM_{sec}$/UVPM and $UVPM_{sec}$/eBC ratios aloft increase markedly, indicating that the elevated UVPM during this period is more strongly influenced by secondary sources. As time progresses, the region characterized by high ratios gradually approaches the ground surface and eventually disappears by 08:00 LT.

The enhanced contribution of secondary sources aloft may be attributed to the increasingly stable stratification after 17:00 LT, which suppresses vertical mixing and inhibits the upward transport of both eBC and UVPM. In contrast, gaseous precursors of $UVPM_{sec}$ (i.e., VOCs) can accumulate above the PBL. Under relatively clean atmospheric conditions with limited condensation sinks, nocturnal chemistry dominated by NO_3^- radicals, together with low ambient temperatures, favors the formation of secondary organic aerosols through gas-to-particle partitioning and temperature-dependent condensation (Han & Jang, 2023; Kuang et al., 2025;

Kulmala, 2022; Morgan et al., 2009; Wang et al., 2023; Zhao et al., 2023b). After sunrise (around 06:00 LT in summer at this site), enhanced solar radiation promotes convective mixing and weakens the nocturnal inversion at the top of the PBL. Consequently, $UVPM_{sec}$-enriched air masses retained within the residual layer are entrained downward into the growing daytime PBL, thereby reducing the concentration gradient between UVPM and eBC within the PBL (Zhao et al., 2023a). In addition, increased human activities and strengthened thermal convection after sunrise lead to larger primary emissions throughout the atmospheric column, causing carbonaceous aerosols to be increasingly dominated by primary components. Because the PBL is still developing at 08:00 LT, the near-surface concentrations of UVPM and eBC are higher than those observed at 05:00 LT. As thermal convection intensifies, the decline in near-surface UVPM and eBC slows between 11:00 and 14:00 LT. Between 14:00 and 17:00 LT, strong convective mixing results in an approximately uniform vertical distribution of both eBC and UVPM from the surface up to ~800 m.

~~This elevated UVPM-to-BC ratio at altitude may be attributable to the lighter molecular weight and smaller size of gas-phase precursors compared to soot particles. Under nocturnal stable stratification, vertical mixing is suppressed, allowing volatile organic compounds (VOCs) to be lofted more readily into the free troposphere. There, in a relatively clean atmosphere lacking efficient coagulation sinks, NO_3^--dominated nighttime chemistry and low temperatures enhance secondary organic aerosol formation via low-temperature condensation and gas–particle partitioning (Han & Jang, 2023; Kuang et al., 2025; Kulmala, 2022; Morgan et al., 2009; Wang et al., 2023; Zhao et al., 2024). These processes collectively amplify the UVPM–BC concentration difference at night. After sunrise, increased solar heating invigorates convection and erodes the nocturnal inversion at the boundary-layer top. Pollutants trapped in the residual layer are then entrained and mixed downward into the daytime boundary layer, reducing the UVPM–BC disparity while both profiles continue to decline with altitude (Zhao et al., 2023). Notably, between 14:00 and 17:00 LST, strong convective mixing homogenizes BC and UVPM within the 100–800 m layer;~~

~~however, BC is not effectively transported to higher altitudes, resulting in a pronounced UVPM–BC difference aloft by 17:00. By approximately 20:00 LST, as convective activity wanes, the UVPM–BC concentration difference reemerges throughout the entire column and remains more pronounced at higher elevations than near the surface.~~

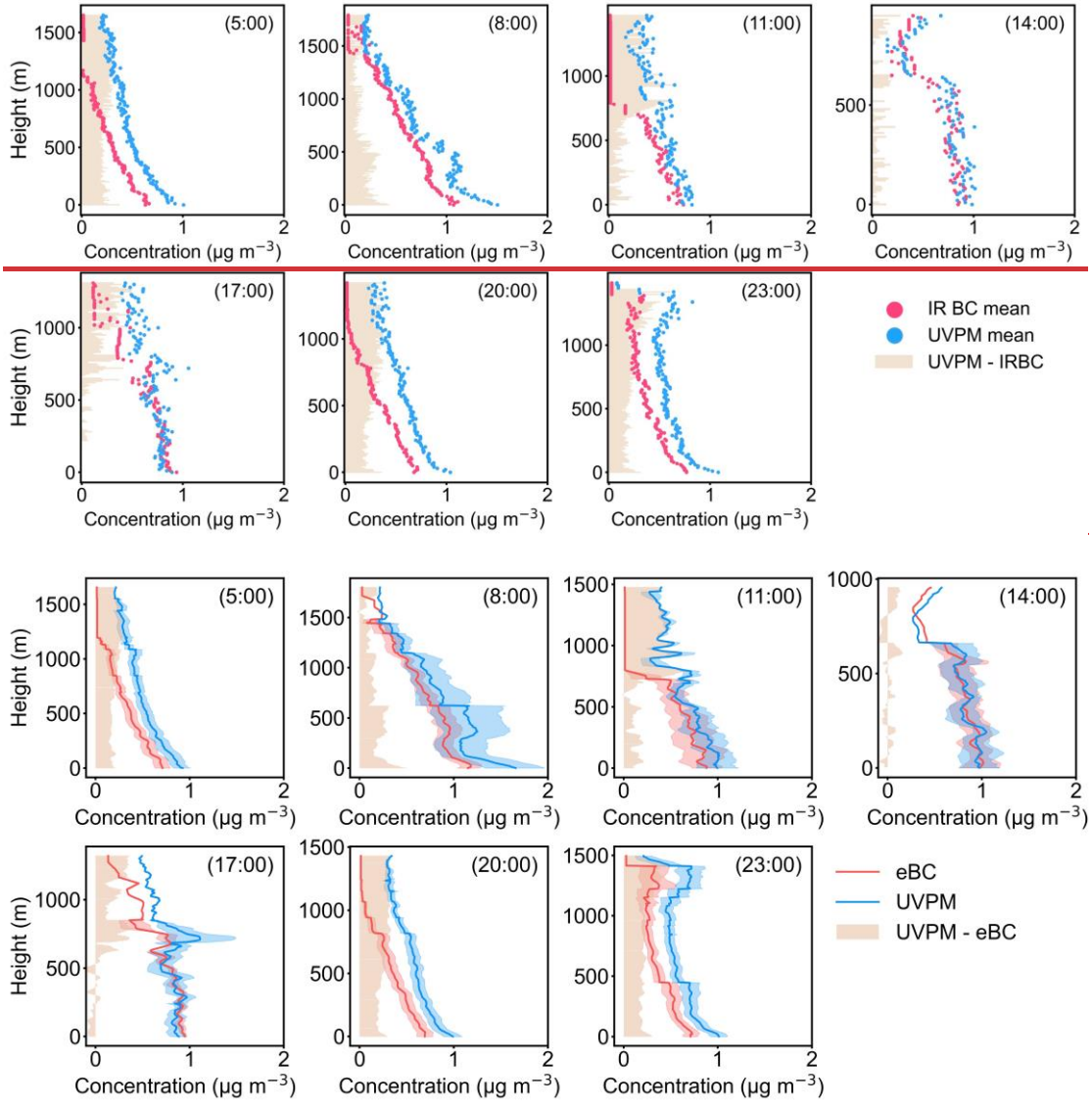

Figure 2. Averaged ~~Diurnal~~ diurnal variation in profiles of the ~~average IR~~eBC and UVPM concentration ~~profiles in~~ during the ~~Pingliang~~ field ~~region~~campaign. The red and blue ~~curve~~lines represent~~s~~ ~~IR~~eBC and UVPM concentrations, respectively, while the red and blue shaded areas denote the standard deviation of eBC and UVPM, respectively. The light orange~~light beige~~ shaded area represents the difference between UVPM and ~~IR~~eBC.

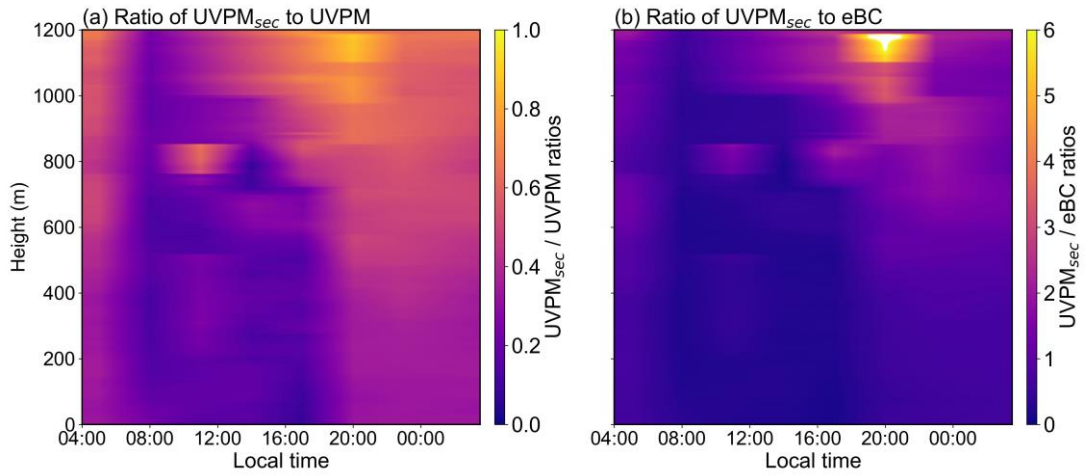

Figure 3. Mean diurnal variations in vertical distribution of a) $UVPM_{sec}$/UVPM and b) $UVPM_{sec}$/eBC ratios during the field campaign.

To better characterize ~~BC~~ vertical structure of UVPM and eBC within the stable ~~boundary layer~~PBL, the observed profiles were classified into four types, each exhibiting distinct features (Details of the method can be found in Text 2 of the Supplementary Material). Regarding the profile clustering presented in Figure 4, the classification was performed by analyzing the vertical change rates (or slopes) of the UVPM and eBC concentrations. These profiles were grouped into four distinct categories: Uniformly decreasing (Cluster 1), Non-uniformly decreasing (Cluster 2), Double-inflection point (Cluster 3), and Continuous increasing (Cluster 4). In Cluster 1, eBC and UVPM decrease almost uniformly with altitude at a rate of approximately 0.51 μg m^{-3} km^{-1} up to 1000 m. Cluster 2 also shows comparable near-surface concentrations of both species, but with a rapid decline of about 1.23 μg m^{-3} km^{-1} below 250 m followed by a more gradual decrease above, reflecting a stronger nocturnal inversion that inhibits upward diffusion. Cluster 3 profiles, typically observed at 05:00, 08:00, and 20:00 L~~S~~T under intense inversions, display a modest decrease of approximately 0.10 μg m^{-3} km^{-1} from the surface to 100 m, an unexpected increase in eBC and UVPM between 100 and 600 m (attributable to pollutant accumulation and upward mixing within the deep neutral residual layer; Kulmala et al., 2023), and a decline above 600 m. In Cluster 4, concentrations remain nearly constant below 200 m but rise with height above this level, likely due to a weak

neutral stratification between 200 and 400 m. Because these observations coincided with strong upper-level winds, measurements above approximately 400 m were curtailed to protect instrumentation, leaving open the question of whether Cluster 4 would exhibit a high-altitude decrease similar to Cluster 3.

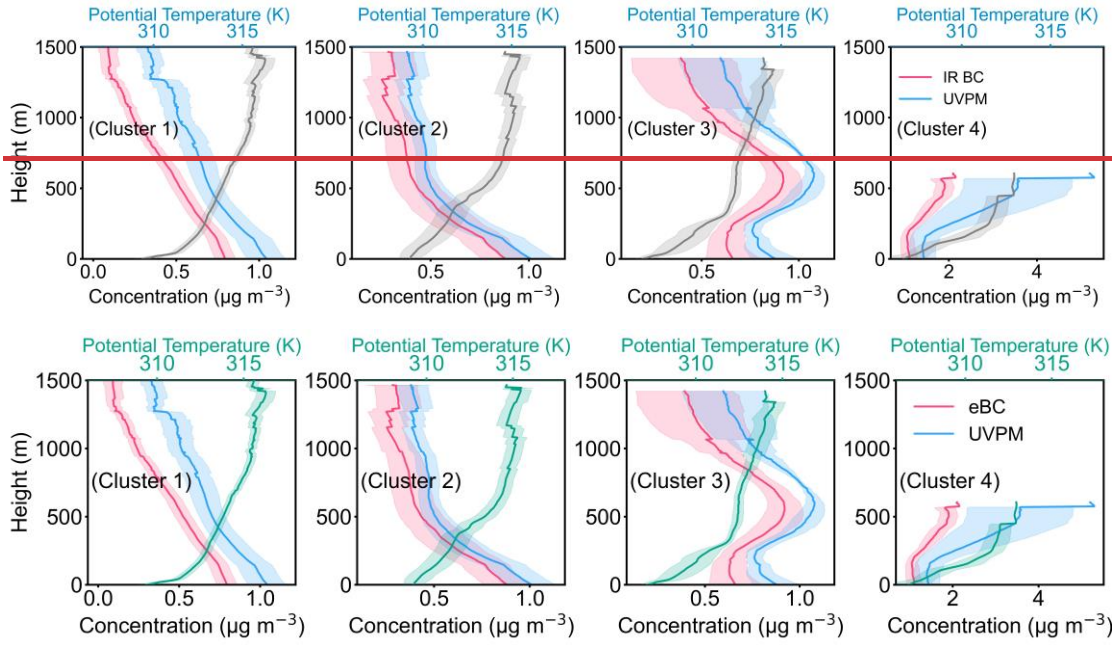

Figure 4. Cluster analysis of UVPM and eBC concentration profiles during the field campaign. The blue, red, and green lines represent the profiles of UVPM, eBC, and potential temperature, respectively, and the shaded areas in the corresponding colors denote their standard deviations.

~~Figure 3. Cluster analysis of BC concentration profiles in the Pingliang region. The red curve represents IRBC, while the blue curve represents UVPM. The red and blue shaded areas indicate the standard errors of IRBC and UVPM, respectively.~~

3.1.3 Diurnal variations of AAE profiles

Figure ~~S5~~ S6 presents the variations of the light absorption coefficients of UVPM and eBC at different altitudes. Overall, both UVPM and eBC absorption coefficients decline steadily with increasing altitude, a pattern primarily controlled by the mass concentrations of carbonaceous aerosols. Moreover, the difference between the UVPM and eBC absorption coefficients diminishes with height, indicating that

UVPM dominates light absorption by carbonaceous aerosols in the lower atmosphere, whereas eBC exerts a greater influence aloft, consistent with the findings of Qi et al. (2025). The AAE, which characterizes the wavelength dependence of the mass-specific absorption by carbonaceous aerosols~~BC~~ (calculation details are given in Figure ~~S6~~S7), was calculated for the study period; the average diurnal AAE values are shown in Figure ~~S7~~S8. Compared with Wu et al. (2021), the AAE of ~~BC~~ carbonaceous aerosols in Pingliang ~~(1.65)~~ is substantially higher than that reported for Shenzhen (<1.00). We further selected observations from representative pollution events to compare AAE under different environmental~~weather~~ conditions (Figure 4~~5~~), Detailed explanations regarding the selection of pollution events are provided in Text 3 of the supplementary material). During dust episodes, AAE increases markedly, by approximately 83% relative to dust-free conditions. Likewise, emissions from diesel vehicles yield higher AAE than periods without diesel vehicles contributions. ~~Under heavy fog in the lowest 200 m, AAE is also elevated; at 200 m the rapid decrease in AAE likely results from the sharp reduction of water vapor aloft. Hence, compared with daytime, the lower frequency and intensity of anthropogenic activity at nighttime lead to a narrower range of aerosol sources and a smaller vertical variation in AAE across the entire profile.~~

Previous studies commonly employ a two-component model to differentiate the Absorption Ångström Exponent of equivalent black carbon (AAE_{eBC}) and brown carbon (AAE_{UVPM}), fixing AAE_{eBC} at 1 and thereby deriving AAE_{UVPM} (Figure S9, the calculation methodology is provided in Text 4 of the supplementary material) (Chen et al., 2015; Chow et al., 2018). ~~.~~Elevated values of AAE_{UVPM} are typically indicative of biomass burning and secondary aging processes (Olson et al., 2015; Gombi et al., 2025). ~~An AAE_{BrC} value greater than 2.0 is generally attributed to biomass burning and secondary aging processes.~~ The diurnal ~~AAE_{BrC}~~ AAE_{UVPM} profiles shown in Figure ~~S8~~ S9 reveal pronounced contributions from secondary organic aerosol formation or from mixed emissions of biomass and fossil fuels at our observation site. Overall, daytime ~~AAE_{BrC}~~ AAE_{UVPM} values exceed those recorded at night and in the

early morning, reflecting the stronger photochemical activity during daylight hours that promotes carbonaceous aerosol aging.

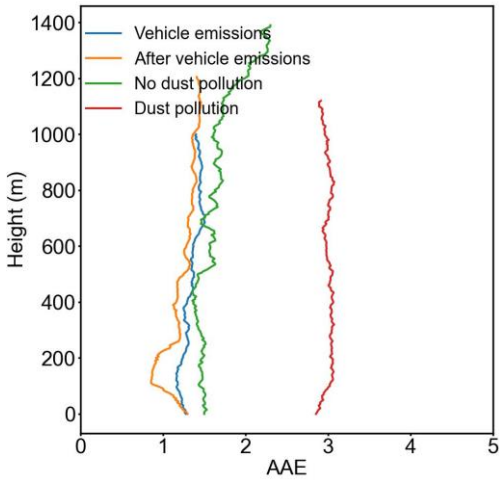

Figure 45. AAE profiles under different pollution conditions. (Diesel Vvehicle emissions, Aafter diesel vehicle emissions, Nno dust pollution, dDust pollution, Heavy fog and No heavy fog occurred at 20:00 on July 17, 2024; 23:00 on July 17, 2024; 08:00 on July 20, 2024; 08:00 on July 21, 2024; 05:00 on July 27, 2024; and 11:00 on July 27, 2024, respectively.).

3.2 Thermodynamic impacts on profiles of eBC and UVPM

Diurnal evolution of the PBLH is one of the primary factors controlling aerosol vertical distribution and is essential for understanding feedbacks between the boundary layerPBL meteorology and aerosols. Zhang et al. (2020) reviewed and compared multiple PBLH retrieval methods. From the perspective of tracer distributions, PBLH inferred from vertical profiles of tracers such as water vapor and aerosols is termed the material PBLH ($PBLH_C$; Shi et al., 2020). Alternatively, PBLH can be derived from the vertical gradient of potential temperature ($PBLH_\theta$), with calculation protocols summarized in Table S1. Because PBLH evolves continuously, we selected a day with uninterrupted observations; however, owing to strong upper-level winds, continuous carbonaceous aerosol profiles were obtained only on 27 July 2024 at seven time slots (Figure 56). Hence, this day serves as a case study for examining how diurnal PBL evolution influences aerosol vertical structure. The parcel method is well suited to convective conditions but cannot accurately resolve $PBLH_\theta$ during early morning and nighttime (Holzworth, 1964), whereas it performs reliably

under strong daytime convection. Using this approach, $PBLH_{\theta}$ at 11:00 and 17:00 LST were 503 m and 459 m, respectively; at 14:00, measurement ceilings did not reach $PBLH_{\theta}$. By contrast, the potential temperature gradient method yields accurate estimates at night and in the early morning: $PBLH_{\theta}$ at 05:00, 08:00, 20:00, and 23:00 LST were 255 m, 181 m, 260 m, and 216 m, respectively. A comparison of UVPM and BC profiles with these $PBLH_{\theta}$ values reveals that nighttime $PBLH_{\theta}$ from potential temperature gradients exceeds the $PBLH_{C}$ inferred from aerosol distributions, a phenomenon also noted by Jiang et al. (2021). This discrepancy arises because nocturnal longwave radiative cooling and weakened turbulence enhance near surface stability and often produce inversions; during their early development, $PBLH_{\theta}$ determined by potential temperature gradients tends to overshoot the inversion top, whereas $PBLH_{C}$ more closely aligns with the inversion height.

Analysis of the potential temperature profiles in Figure 5 6 indicates that at around 05:00 LST the planetary boundary layerPBL top lay near 260 m. Below this altitude, both eBC and UVPM concentrations decrease slightly with height. The potential temperature profile further reveals a deep residual layer above the PBLboundary layer top, where colder near-surface air is trapped beneath warmer air aloft, creating a stable stratification that inhibits mixing within that layer and leads to increasing particle concentrations toward its base. In the transition to the free troposphere above the residual layer, comparatively low aerosol concentrations and enhanced turbulence promote further dilution, and beyond approximately 500 m eBC and UVPM again decline with height. By 08:00 LST the PBLboundary layer height remained near 200 m, and the vertical variation in aerosol concentrations mirrored the pattern observed at 05:00. With increasing solar insolation, however, surface heating intensified convection so that by 11:00 LST the PBL boundary layer top had risen to roughly 500 m. During this stage, relatively small vertical gradients in eBC and UVPM within the boundary layerPBL indicate well-mixed conditions. At 14:00 LT tethered-balloon

sampling did not reach the PBL top, but observations within the PBL show uniform aerosol distributions, preventing a direct assessment of PBLH effects on concentration profiles. The potential- temperature gradients between 11:00 and 14:00 L~~S~~T exhibit significant fluctuations, signaling unstable stratification favorable to vertical pollutant transport (Li, 2019). From 14:00 to 17:00 L~~S~~T, as solar radiation waned and surface temperatures fell, the PBL~~boundary layer~~ top subsided to about 450 m. At this time, potential temperatures within the ~~boundary layer~~PBL remained lower than at the surface and displayed pronounced variability, reflecting continued unstable stratification and strong vertical mixing; eBC and UVPM maintained nearly uniform distributions. Above the ~~boundary layer~~PBL, a mixed layer approximately 300 m thick persisted; at its top, diminished turbulence inhibited aerosol dispersion, causing localized accumulation of eBC and UVPM (Ding et al., 2016). By 20:00 L~~S~~T, sunset-driven surface cooling weakened convection, a nocturnal temperature inversion developed near the ground, and calm winds led to pollutant accumulation at low altitudes. As surface temperatures continued to drop, vertical transport further diminished, confining aerosols below roughly 200 m by 23:00 L~~S~~T.

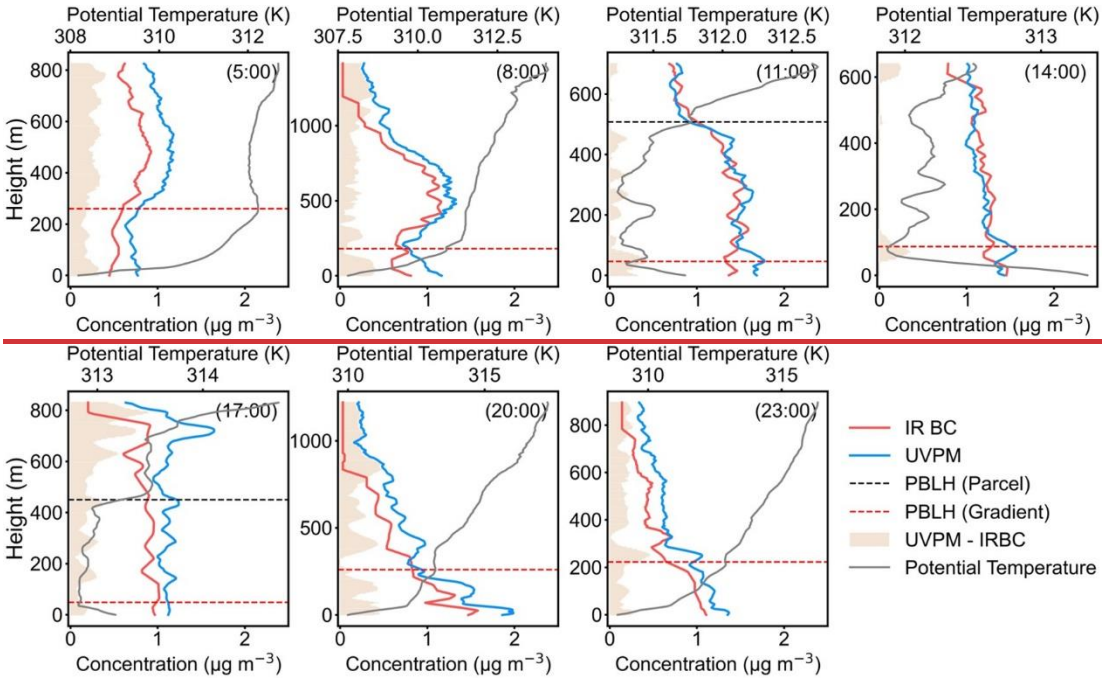

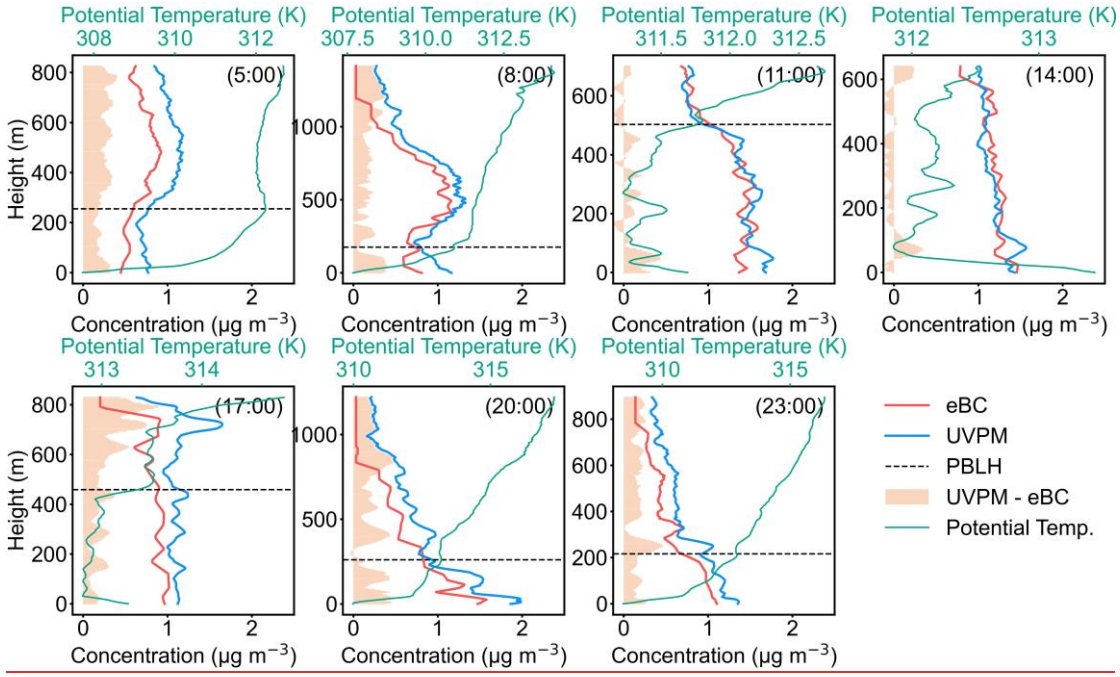

Figure 6. Diurnal variations in profiles of eBC, UVPM and potential temperature on July 27, 2024. The red line represents eBC, the blue line represents UVPM, and the green line represents the potential temperature profile. The light orange shaded area represents the difference between UVPM and eBC. The black dashed lines represent the PBLH.

~~Figure 5. Diurnal variations of BC, UVPM and potential temperature profiles on July 27, 2024. The red curve represents IRBC, the blue curve represents UVPM, and the gray curve represents the potential temperature profile. The light beige shaded area represents the difference between IRBC and UVPM. The black and red dashed lines represent the PBLH calculated using the air parcel method and the potential temperature gradient method, respectively.~~

3.3 Dynamic impacts on profiles of eBC and UVPM

3.3.1 Impacts of long-range transport on carbonaceous aerosols

Long-range transport of air masses plays a crucial role in shaping the vertical distribution of air pollutants. Figure ~~S9~~ S10 presents the 500 m backward trajectories and their altitude profiles for air masses arriving at the site during the observation period, and Figure S11 presents temporal variation in the PBLH of the nearest urban area of Pingliang during the observation period. Figure S11~~t~~ shows that, upon

entering the Pingliang region, these air parcels generally descend to below ~~1500 m~~PBLH, meaning that, in addition to pollutants carried within the air mass itself, emissions from surrounding urban areas also significantly impact the receptor site. Trajectory-cluster analysis at 100 m, 500 m, and 1000 m (Figure ~~6~~7) reveals that, in summer, Pingliang is principally influenced by air masses originating from Inner Mongolia and Ningxia to the north, from Gansu–Qingyang and northern Shaanxi to the east, and from southern Shaanxi to the south. At 500 m and 1000 m, regional contributions from these directions are broadly similar, whereas at 100 m the proportion of short-range flow from the southeast increases markedly. The shaded overlays in Figure ~~6~~ 7 show the weighted potential source contribution function (WPSCF) and weighted concentration-weighted trajectory (WCWT) results for UVPM. WPSCF indicates that air parcels from Inner Mongolia, Ningxia, Shanxi, and Shaanxi to the north, east, and south exert the greatest influence on the Pingliang site. Specifically, at 100 m the highest WPSCF values are located in the local Pingliang area and ~~occur along~~ the Shaanxi–Gansu border region, while at 500 m parcels from central Shaanxi and the Shanxi–Henan–Shaanxi nexus dominate, followed by the tri-provincial junction of Shaanxi, Gansu, and Sichuan. The WCWT analysis yields results similar to those of the WPSCF, but it additionally highlights that southern Shaanxi is also an important source region of UVPM at the observation site.~~However, the CWT analysis identifies Hanzhong in southern Shaanxi as the most significant source region for UVPM at the receptor.~~ Taken together, WPSCF and WCWT pinpoint southern Shaanxi cities and local emissions around Pingliang as major contributors to carbonaceous aerosol pollution, whereas at higher altitudes UVPM is primarily transported from the south. ~~Overall, these source-apportionment results align with the conditional probability function (CPF) analysis, confirming that southerly flows contribute most substantially to UVPM concentrations at the observation site.~~

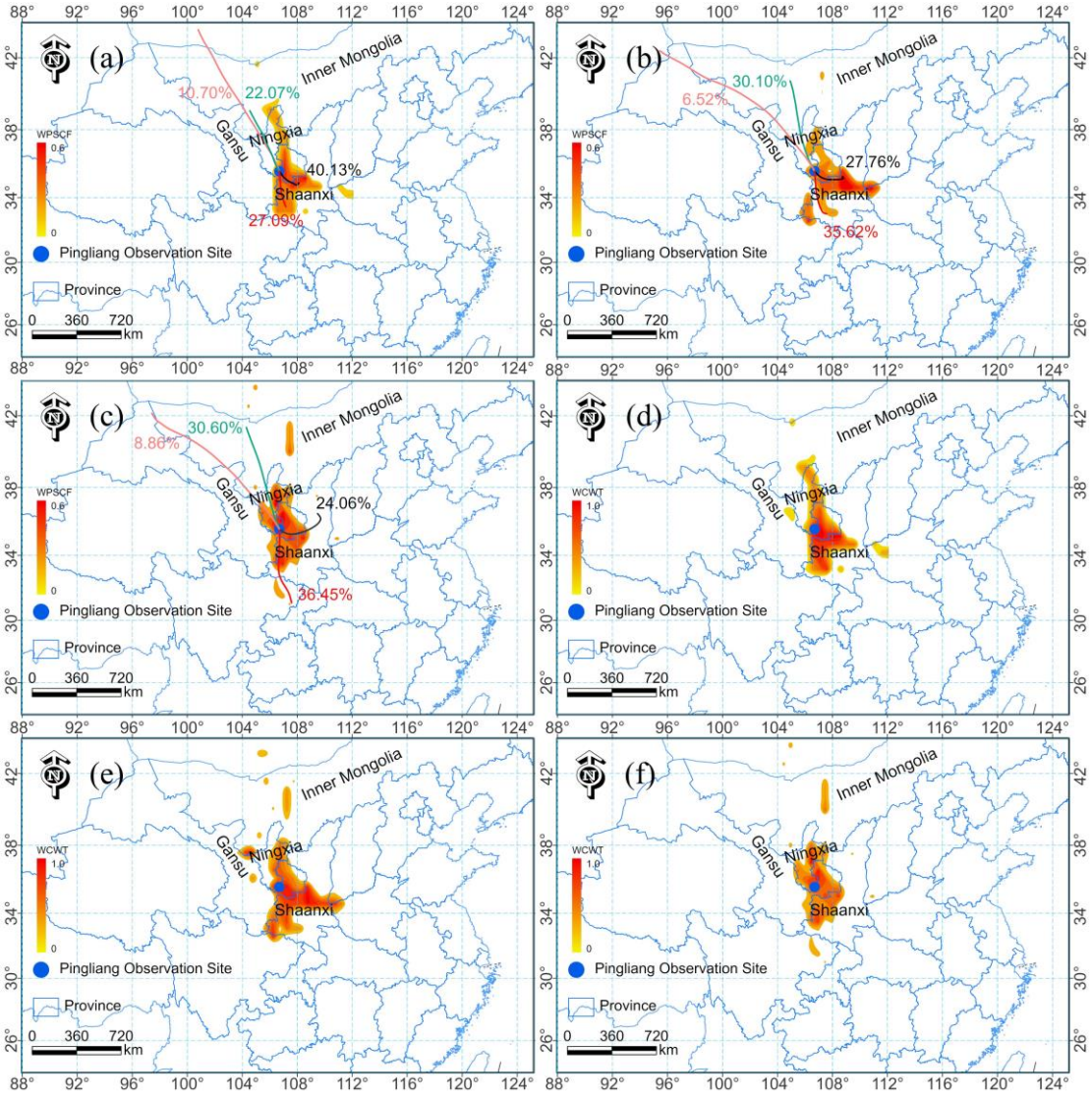

Figure ~~6~~7. Backward trajectory clustering and WPSCF analysis results of air masses at heights of a) 100 m, b) 500 m, and c) 1000 m during the observation period, respectively. WCWT analysis results of air masses at heights of d) 100 m, e) 500 m, and f) 1000 m during the observation period, respectively.

3.3.2 Impacts of local sources on carbonaceous aerosols

In addition to long-range transport, local wind speed and direction significantly modulate the vertical distribution of aerosols at the observation site. Conditional Probability Function (CPF) plots, which relate pollutant concentrations to wind sectors and speeds, help elucidate these local transport and dispersion mechanisms. Figure 8 shows CPF diagrams for the 90th percentile of UVPM and eBC concentrations at 100 m, 500 m and 1000 m. The mean UVPM concentrations

decrease with altitude, from 0.86 μg m^{-3} at 100 m, to 0.63 μg m^{-3} at 500 m, and to 0.44 μg m^{-3} at 1000 m, indicating that extreme UVPM events become less probable at higher altitudes. At 100 m, elevated UVPM concentrations are associated with southerly, southwesterly, southeasterly, northerly, and northwesterly winds, reflecting the combined influence of urban emissions and local rural emissions surrounding the observation site. At 500 m, the influence of northwesterly, southwesterly and northerly sectors diminishes, while southerly winds remain the dominant driver of high UVPM, albeit with reduced effect. Southeasterly winds occasionally lead to relatively high UVPM values at both 100 m and 500 m altitude, although this occurrence is less frequent, which is consistent with the results of backward trajectories. We hypothesize that this variability may be associated with local and sporadic emissions from residents in the vicinity, as the observation site is located in a rural area with no stationary point sources. However, the specific cause cannot be definitively determined by the CPF alone. We will continue to analyze this phenomenon in subsequent observational studies to provide a clearer explanation.

The analysis of eBC shows results similar to those of UVPM. The main difference is that at 500 m and 1000 m, southeasterly winds exert a slightly stronger influence on UVPM than on eBC. In addition, the relationships between UVPM (or eBC) and wind direction and speed at different altitudes indicate that carbonaceous aerosols at 100 m above the observation site are highly sensitive to almost all wind directions. This is primarily because pollutants at this height are strongly affected by local emissions from rural areas surrounding the site. In contrast, at 500 m and 1000 m, carbonaceous aerosol concentrations exhibit a pronounced association with southerly and southeasterly winds, while their dependence on other wind directions weakens. This indicates that transport from the south and southeast is the significant source of the carbonaceous aerosol burden above the observation site, a pattern that is also reflected in the WPSCF and WCWT results shown in Figure 7. In addition, this may also be related to the fact that Pingliang urban area is located south of the observation site (Figure 1).~~Figure 7 shows CPF diagrams for the 90th percentile of UVPM~~

~~concentrations at 100 m, 500 m and 1000 m. The mean UVPM concentrations decrease with altitude, from 0.64 μg m^{-3} at 100 m, to 0.44 μg m^{-3} at 500 m, and to 0.31 μg m^{-3} at 1000 m, indicating that extreme UVPM events become less probable aloft. At 100 m, elevated UVPM levels are associated with southerly, southwesterly, northerly and northwesterly winds, reflecting both urban emissions and regional inflow. At 500 m, the influence of northwesterly, southwesterly and northerly sectors diminishes, while southerly winds remain the dominant driver of high UVPM, albeit with reduced effect. Southeasterly winds sporadically produce high UVPM at both 100 m and 500 m, likely linked to local point sources, but occur infrequently. Overall, southerly and southeasterly sectors exert the greatest influence on UVPM at all levels, consistent with the location of Pingliang's urban center directly south of the measurement site (Figure 1).~~

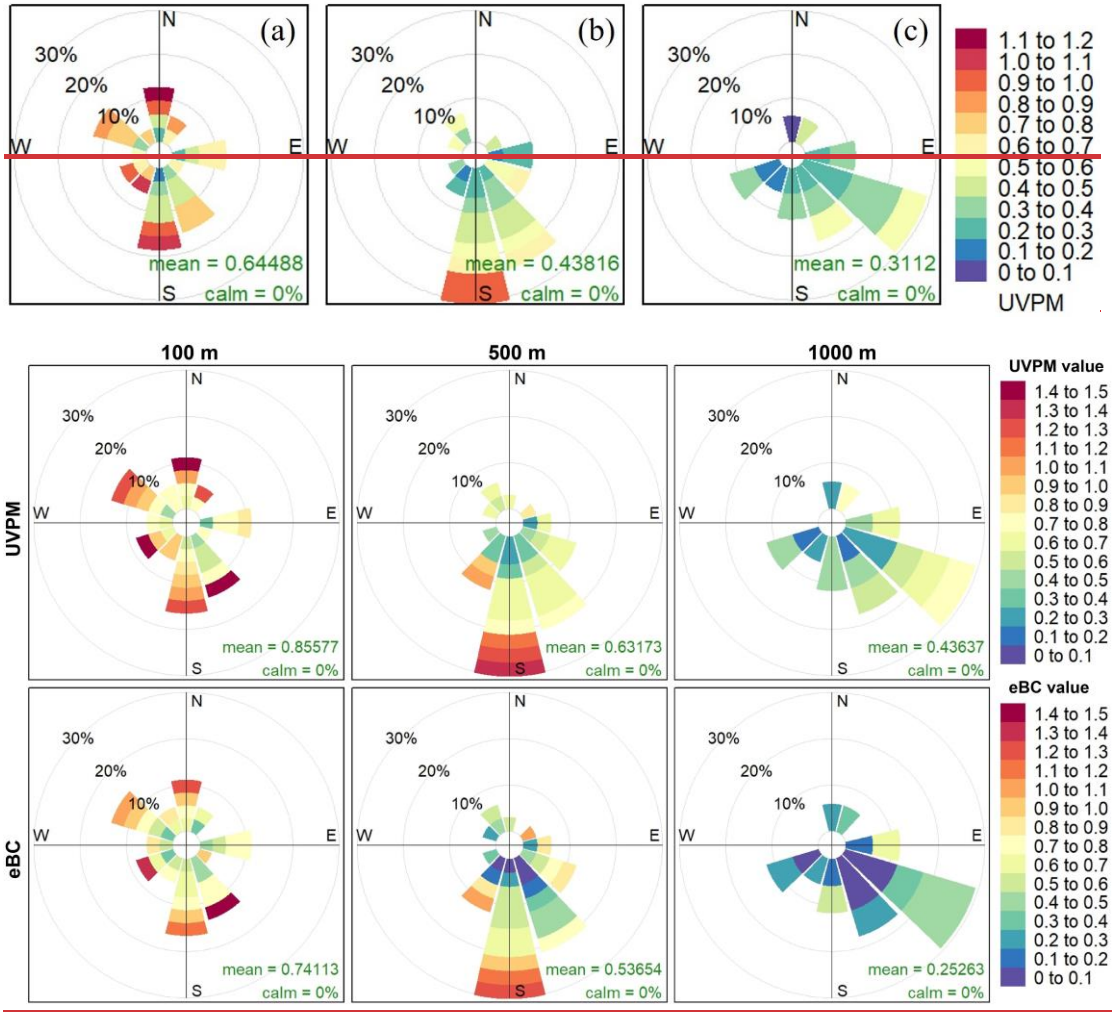

Figure 8. Conditional probability function (CPF) diagrams of the 90th percentile of the

UVPM and eBC concentrations with respect to wind speed and direction at the heights of 100 m, 500 m and 1000 m above ground level.

~~Figure 7. CPF (Conditional Probability Function) diagrams of the 90th percentile of the UVPM concentration with respect to wind speed and wind direction at the heights of a) 100, b) 500 and c) 1000 m.~~

To better compare the thermodynamically driven and dynamically driven influences on pollutant vertical distribution, this section again focuses on 27 July 2024 to examine the effects of wind speed and mechanical turbulence. Figure ~~8~~ 9 presents horizontal and vertical wind speeds together with mechanical turbulence measured by the Doppler wind lidar during the sampling periods on that day. At 05:00 L~~S~~T, both horizontal and vertical wind speeds within the ~~boundary layer~~PBL were low, while mechanical turbulence was comparatively high, promoting efficient vertical mixing and producing a nearly uniform distribution of carbonaceous aerosol concentrations throughout the ~~boundary layer~~PBL (Figure 6). In the residual layer above, stronger vertical winds combined with weaker turbulence transported aerosols upward, causing UVPM and eBC concentrations to increase with height between 400 and 600 m. At 08:00 L~~S~~T, residual-layer concentrations exhibited a pattern similar to that at 05:00, but stronger vertical winds and reduced turbulence at the residual-layer top led to a more pronounced concentration decrease above the layer. By late morning, enhanced vertical wind speeds within the ~~boundary layer~~PBL facilitated upward transport of pollutants. However, at both 11:00 and 14:00 L~~S~~T the aerosol concentration profile remained relatively uniform, with only a slight decrease with height; this reflects the competing effects of thermal convection, which lifts near-surface pollutants, and elevated turbulence aloft, which strengthens vertical exchange. At 17:00 L~~S~~T, subsiding motions prevailed at 900 – 1200 m and mechanical turbulence index throughout the column was low, weakening vertical exchange and causing pollutants to accumulate near 800 m. By 20:00 L~~S~~T, weak mechanical turbulence at the ~~boundary layer~~PBL top and widespread subsidence near the surface suppressed

upward transport of carbonaceous aerosols; as a result, pollutant concentrations decreased sharply with height within the ~~boundary layer~~PBL, while above the ~~boundary-layer~~PBL top horizontal and vertical winds aided dispersion, producing a continued decline in aerosol concentrations up to 800 m.

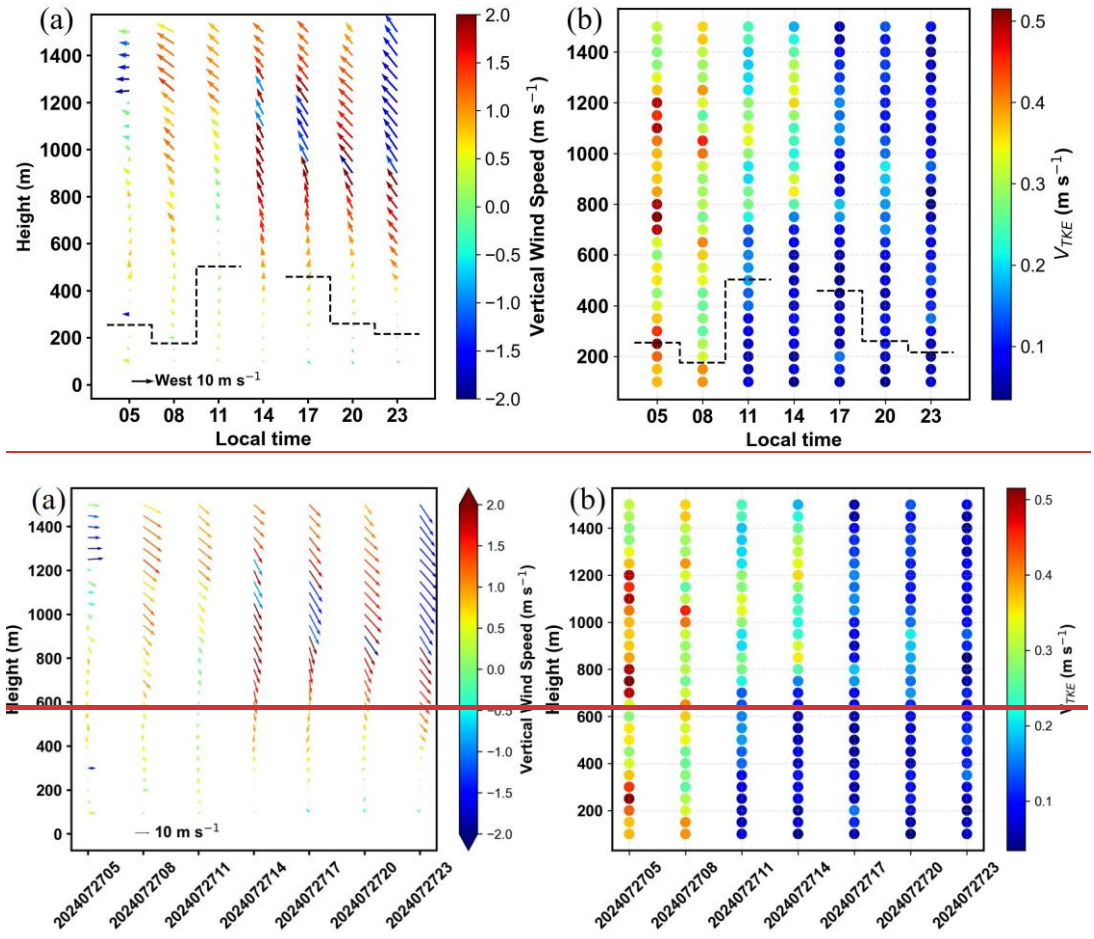

Figure 9. a) Vertical wind speed, horizontal wind speed, and wind direction at heights of 100 – 1500 m during different periods on July 27, 2024 (The direction of the arrow represents the wind vector direction, i.e., a rightward arrow represents a westerly wind). The height resolution for wind direction and speed is 50 m, and the length of the arrow represents the magnitude of the horizontal wind speed. The color of the arrows represents the vertical wind speed. b) V_{TKE} values at different heights (calculated based on wind speed data within 5 min), where different colors represent different V_{TKE} values. The black dashed line in the figure represents the PBLH during the observation period.

~~Figure 8. a) Vertical wind speed, horizontal wind speed and direction at 100–1500 m at the~~

~~varying hours on July 27, 2024. The arrows indicate horizontal wind direction, with arrows pointing upward representing northerly winds. Arrow length represents horizontal wind speed magnitude. The color-shaded areas represent vertical wind speed. b) The V_{TKE} values at varying altitudes, with distinct colors representing different V_{TKE} values.~~

To systematically investigate the mechanisms by which thermodynamic and dynamic processes influence the vertical distribution of carbonaceous aerosols, the observation periods were grouped into daytime (8:00, 11:00, 14:00 and 17:00 L~~S~~ST) and nighttime (20:00, 23:00 and 5:00 L~~S~~ST). A random forest nonlinear regression was applied to quantify the relative contributions of thermal forcing and dynamic forcing to the vertical concentration gradients of carbonaceous aerosols at different altitude layers (Figure ~~9~~10). All regressions achieved coefficients of determination (R^2) above 0.70, indicating good explanatory power. During daytime, these two processes exhibit clear vertical stratification. From the surface up to 600 m, thermal forcing dominates the evolution of aerosol concentration, whereas between 600 m and 1000 m horizontal wind speed is the primary driver. At night, the influence of thermal forcing is more complex. Between the surface and 300 m both thermal forcing and horizontal wind speed jointly govern vertical concentration variability. Between 300 m and 500 m, thermal forcing alone exerts decisive control, while above 500 m dynamic processes exert a much stronger influence than thermodynamic processes. Comparison with ~~boundary layer height~~PBLH analyses shows that 300 m corresponds to the inversion top at night, where both thermodynamic and dynamic mechanisms contribute comparably to aerosol pollution. The layer from 300 m to 500 m largely coincides with the residual layer, which retains daytime turbulence characteristics and therefore responds more sensitively to thermal forcing. It should be noted that daytime measurements were taken at 08:00, 11:00 and 17:00 L~~S~~ST, a period when the ~~boundary layer~~PBL had not yet fully developed, so that 600 m approximately corresponds to the daytime ~~boundary layer~~PBL top. Consequently, the vertical distribution of carbonaceous aerosols within the daytime PBL is primarily governed by thermodynamic processes, in contrast to the combined dynamic and thermodynamic

control that dominates within the nocturnal residual layer. ~~Consequently, within the daytime boundary layer, carbonaceous aerosol vertical distributions are mainly controlled by thermodynamic processes, in contrast to the thermodynamic dominance within the nocturnal residual layer.~~ A schematic of these regulatory mechanisms for aerosol vertical structure is presented in Figure ~~10~~11.

Li et al. (2019) also found through radiosonde observations that during the daytime, thermodynamic processes induced unstable stratification within the ~~boundary layer~~PBL, resulting in well-mixed aerosols. In contrast, at night, the stable atmospheric stratification from the surface to 200 meters suppressed vertical dispersion of aerosols. Between 500 and 1000 meters, the presence of a low-level jet significantly influenced the vertical distribution of aerosols. In addition, strong mechanical turbulence played a key role in facilitating aerosol dispersion near the top of the ~~boundary layer~~PBL (Sun et al., 2024). These findings are consistent with the conclusions of this study.

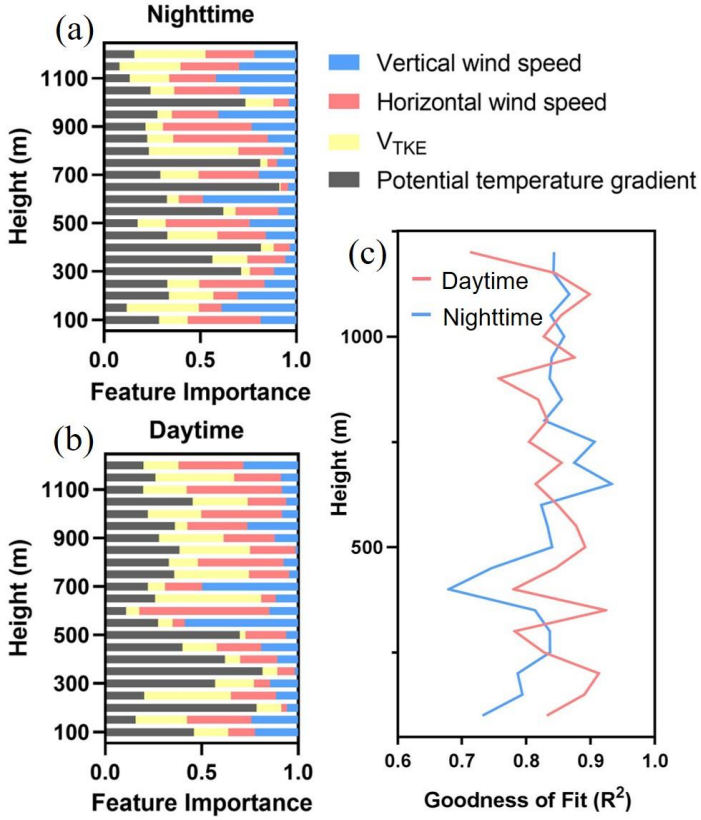

Figure ~~9~~10. Results of feature importance analysis for the impacts of potential temperature

gradient, mechanical turbulence, horizontal wind speed, and vertical wind speed on the UVPM gradient during a) nighttime and b) daytime, respectively. c) model goodness of fit (R^2) in the calculation.

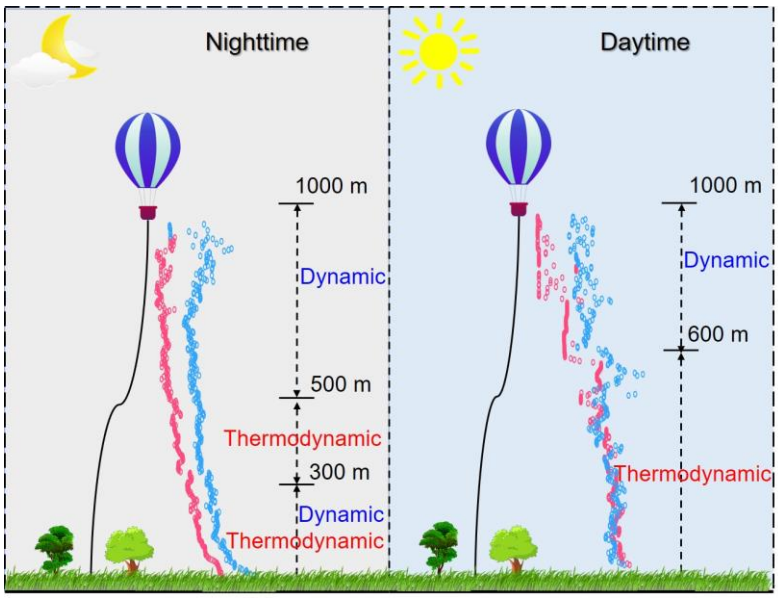

Figure ~~10~~11. Schematic illustration of thermodynamic and dynamic impacts on aerosol vertical distribution. Within the figure, red circles denote ~~IR~~ eBC concentrations, whereas blue circles denote UVPM concentrations; the more rightward a circle's position, the higher the corresponding concentration.

4. Conclusions

Pingliang City is situated on the Loess Plateau in northwestern China, where observational data on the vertical distribution of carbonaceous aerosols and meteorological parameters within the planetary boundary layer remain limited. To address this data gap, this study conducted detailed vertical profiling in a typical tableland region of the Loess Plateau using tethered balloons equipped with relevant observation instruments during July 2023 and July 2024.

The study found that near-surface concentrations of black carbon (eBC) and ultraviolet-absorbing particulate matter (UVPM) in Pingliang were 0.84 μg m^{-3} and

1.24 μg m^{-3}, respectively~~0.10 μg m^{-3} and 0.12 μg m^{-3}, respectively~~. These concentrations are slightly lower than those reported for major Chinese cities including Beijing, Shanghai, Nanjing, Chengdu, Shenzhen, Hengshui, the Beibu Gulf region, and Lanzhou, as well as European cities such as Stuttgart in Germany and Milan in Italy. However, they are higher than the eBC levels observed over the Tibetan Plateau and in the Arctic. A comparison of the vertical profiles of eBC and UVPM showed that during early morning and nighttime periods, when convective activity is relatively weak, UVPM concentrations in the upper atmosphere are generally higher than those of eBC. Near the surface, the difference between eBC and UVPM concentrations is relatively small. This phenomenon is likely related to the formation of new particles in the upper atmosphere through gas to particle conversion of gaseous pollutants.

Analysis of thermodynamic and dynamic processes influencing the vertical distribution of carbonaceous aerosols shows that thermodynamic processes primarily govern vertical transport in the near-surface layer, while enhanced dynamic processes in the upper atmosphere promote horizontal dispersion of pollutants. The influence of thermodynamic and dynamic mechanisms on aerosol vertical profiles exhibits distinct stratification between daytime and nighttime. At various altitudes, air masses originating from the south are consistently associated with elevated UVPM concentrations. This pattern may be attributed to the combined influence of pollution sources located in the urban area to the south of the site and topographic differences along the north and south directions.

Nevertheless, there are still some limitations in this study that should be addressed in future work. Firstly, observations under strong wind conditions in the upper air were not successfully conducted during the campaign. Secondly, the study primarily focused on a limited set of air pollutants. Future research will incorporate additional gaseous pollutants such as SO_2, NO_2, O_3, and VOCs to enable a more comprehensive analysis of the chemical formation mechanisms and vertical distribution

characteristics of aerosols. Furthermore, the filed campaign was conducted at only a site, and thus the feedbacks between aerosols and the PBL meteorology cannot be fully ~~understanded~~understood at whole Loess Plateau. The upcoming field campaign will be conducted at the other sites to better reveal the impact of thermodynamic and dynamic processes on the vertical profiles of air pollutants.

Author contributions. QS performed the data analysis and prepared the initial draft of the manuscript. SZ and YY designed the experimental approach and revised the manuscript. QS, SZ, LD, TZ, GZ, JL, XZ, and YL participated in data collection during the experiment.

Code/Data availability.

The air pollution data were downloaded from the China Environmental Meteorological Data Service Platform (http://eia-data.com/), and the station ID for Pingliang City is 2656A. The GDAS1 meteorological fields used to drive the backward trajectory calculations were obtained from the NOAA FTP repository (ftp://arlftp.arlhq.noaa.gov/pub/archives/gdas1). Raw data sets (Qi et al., 2025, https://doi.org/10.5281/zenodo.17947573) used in this paper are available at https://zenodo.org/records/17947573 (last access: 16 December 2025).

~~The code and data used in this work can be accessed by contacting the corresponding author.~~

Financial support. This work was supported by the National Natural Science Foundation of China (42422504), Major Science and Technology Project of Gansu Province (24ZD13FA003), and Excellent Member of Youth Innovation Promotion Association, Chinese Academy of Sciences (Y2021111)~~, and Youth United Funding of Lanzhou Branch of Chinese Academy of Sciences~~.

References:

Allen, R. J., Landuyt, W. The vertical distribution of black carbon in CMIP5 models: Comparison to observations and the importance of convective transport. J. Geophys. Res.-Atmos., 119(8), 4808-4835, http://doi.org/10.1002/2014JD021595, 2014.

Ångström, A., 1929. On the atmospheric transmission of sun radiation and on dust in the air. Geogr. Ann. 11, 156–166.

Bisht, D. S., Tiwari, S., Dumka, U. C., Srivastava, A. K., Safai, P. D., Ghude, S. D., Chate, D. M., Rao, P. S. P., Ali, K., Prabhakaran, T., Panickar, A. S., Soni, V. K., Attri, S. D., Tunved, P., Chakrabarty, R. K., Hopke, P. K. Tethered balloon-born and ground-based measurements of black carbon and particulate profiles within the lower troposphere during the foggy period in Delhi, India. Sci. Total Environ., 573, 894-905, http://doi.org/10.1016/j.scitotenv.2016.08.185, 2016.

Bond, T. C., Doherty, S. J., Fahey, D. W., Forster, P. M., Berntsen, T., DeAngelo, B. J., Flanner, M. G., Ghan, S., Kärcher, B., Koch, D., Kinne, S., Kondo, Y., Quinn, P. K., Sarofim, M. C., Schultz, M. G., Schulz, M., Venkataraman, C., Zhang, H., Zhang, S., Bellouin, N., Guttikunda, S. K., Hopke, P. K., Jacobson, M. Z., Kaiser, J. W., Klimont, Z., Lohmann, U., Schwarz, J. P., Shindell, D., Storelvmo, T., Warren, S. G., Zender, C. S. Bounding the role of black carbon in the climate system: A scientific assessment. J. Geophys. Res.-Atmos., 118(11), 5380-5552, http://doi.org/10.1002/jgrd.50171, 2013.

Chen, D. L., Liao, H., Yang, Y., Chen, L., Zhao, D. L., Ding, D. Simulated impacts of vertical distributions of black carbon aerosol on meteorology and $PM_{2.5}$ concentrations in Beijing during severe haze events. Atmos. Chem. Phys., 22(3), 1825-1844, http://doi.org/10.5194/acp-22-1825-2022, 2022.

Chen, L.W.A., Chow, J.C., Wang, X.L., Robles, J.A., Sumlin, B.J., Lowenthal, D.H., Zimmermann, R., Watson, J.G. Multi-wavelength optical measurement to enhance thermal/optical analysis for carbonaceous aerosol. Atmos. Meas. Tech., 8(1), 451-461, https://doi.org/10.5194/amt-8-451-2015, 2015.

Chow, J.C., Watson, J.G., Green, M.C., Wang, X.L., Chen, L.-W.A., Trimble, D.L., Cropper, P.M., Kohl, S.D., Gronstal, S.B. Separation of brown carbon from black carbon for IMPROVE and CSN PM2.5 samples, Air Waste Manag. Assoc., 68(5), 494-510, https://doi.org/10.1080/10962247.2018.1426653, 2018.

Ding, A. J., Huang, X., Nie, W., Sun, J. N., Kerminen, V. M., Petäjä, T., Su, H., Cheng, Y. F., Yang, X. Q., Wang, M. H., Chi, X. G., Wang, J. P., Virkkula, A., Guo, W. D., Yuan, J., Wang, S. Y., Zhang, R. J., Wu, Y. F., Song, Y., Zhu, T., Zilitinkevich, S., Kulmala, M., Fu, C. B. Enhanced haze pollution by black carbon in megacities in China. Geophys. Res. Lett., 43(6), 2873-2879, http://doi.org/10.1002/2016GL067745, 2016.

Emeis, S., Schaefer, K., Muenkel, C. Surface-based remote sensing of the mixing-layer height - a review. Meteorol. Z., 17(5), 621-630, http://doi.org/10.1127/0941-2948/2008/0312, 2008.

Ferrero, L., Cappelletti, D., Busetto, M., Mazzola, M., Lupi, A., Lanconelli, C., Becagli, S., Traversi, R., Caiazzo, L., Giardi, F., Moroni, B., Crocchianti, S., Fierz, M., Močnik, G., Sangiorgi, G., Perrone, M. G., Maturilli, M., Vitale, V., Udisti, R., Bolzacchini, E. Vertical profiles of aerosol and black carbon in the Arctic: a seasonal phenomenology along 2 years (2011–2012) of field campaigns. Atmos. Chem. Phys., 16(19), 12601-12629, http://doi.org/10.5194/acp-16-12601-2016, 2016.

Ferrero, L., Mocnik, G., Ferrini, B. S., Perrone, M. G., Sangiorgi, G., Bolzacchini, E. Vertical profiles of aerosol absorption coefficient from micro-Aethalometer data and Mie calculation over Milan. Sci. Total Environ., 409(14), 2824-2837, http://doi.org/10.1016/j.scitotenv.2011.04.022, 2011.

Gombi, C., Rahman, A., Hodovány, S. et al. A demonstrative study of a novel approach for spectral based source apportionment of ambient aerosols. Sci. Rep., 15, 19501, https://doi.org/10.1038/s41598-025-04022-3, 2025.

Guagenti, M. and Dexheimer, D. and Ulinksi, A. and Walter, P. and Flynn III, J. H. and Usenko, S. A modular approach to volatile organic compound samplers for tethered balloon and drone platforms. Atmos. Meas. Tech., 18(9), 2125-2136, https://doi.org/10.5194/amt-18-2125-2025, 2025.

Guan, X., Zhang, N. Y., Tian, P. F., Tang, C. G., Zhang, Z. D., Wang, L. G., Zhang, Y. S., Zhang, M., Guo, Y. M., Du, T., Cao, X. J., Liang, J. N., Zhang, L. Wintertime vertical distribution of black carbon and single scattering albedo in a semi-arid region derived from tethered balloon observations. Sci. Total Environ., 807, http://doi.org/10.1016/j.scitotenv.2021.150790, 2022.

Gutzler, D. S. Climatic variability of temperature and humidity over the tropical western Pacific. Geophys. Res. Lett., 19(15), 1595-1598, https://doi.org/10.1029/92GL01579, 1992.

Hagler, G. S. W., Yelverton, T. L. B., Vedantham, R., Hansen, A. D. A., Turner, J. R. Post-processing Method to Reduce Noise while Preserving High Time Resolution in Aethalometer Real-time Black Carbon Data. Aerosol Air Qual. Res., 11(5), 539-546, http://doi.org/10.4209/aaqr.2011.05.0055, 2011.

Han, S., Jang, M. Modeling daytime and nighttime secondary organic aerosol formation via multiphase reactions of biogenic hydrocarbons. Atmos. Chem. Phys., 23(2), 1209-1226, http://doi.org/10.5194/acp-23-1209-2023, 2023.

Han, Y., Zhou, Y. W., Guo, J. P., Wu, Y. H., Wang, T. J., Zhuang, B. L., Li, M. M. The Characteristics of Spatial and Temporal Variations in the PBL during the Landfall of Tropical Cyclones across East China. J. Appl. Meteorol. Clim., 58(7), 1557-1572, http://doi.org/10.1175/JAMC-D-18-0131.1, 2019.

Hodnebrog, O., Myhre, G., Samset, B. H. How shorter black carbon lifetime alters its climate effect. Nat. Commun., 5(5), 7. http://doi.org/10.1038/ncomms6065, 2014.

Holzworth, G. C. Estimates of mean maximum mixing depths in the contiguous united states. Mon. Weather Rev., 92(5), 235-242, http://doi.org/10.1175/1520-0493(1964)092<0235:EOMMMD>2.3.CO;2, 1964.

~~Jiang, Y. Y., Xin, J. Y., Zhao, D. D., Jia, D. J., Tang, G. Q., Quan, J. N., Wang, M., Dai, L. D. Analysis of differences between thermodynamic and material boundary layer structure: Comparison of detection by ceilometer and microwave radiometer. Atmos. Res., 248, 105179, http://doi.org/10.1016/j.atmosres.2020.105179, 2021.~~

Kroll, J., Donahue, N., Jimenez, J. Kessler, S., Canagaratna, M., Wilson, K., Altieri, K., Mazzoleni, L., Wozniak, A., Bluhm, H., Mysak, E., Smith, J., Kolb, C., Worsnop, D. Carbon oxidation state as a metric for describing the chemistry of atmospheric organic aerosol. *Nature Chem.*, 133–139, https://doi.org/10.1038/nchem.948, 2011.

Kuang, Y., Luo, B., Huang, S., Liu, J. W., Hu, W. W., Peng, Y. W., Chen, D. H., Yue, D. L., Xu, W. Y., Yuan, B., Shao, M. Formation of highly absorptive secondary brown carbon through nighttime multiphase chemistry of biomass burning emissions. Atmos. Chem.

Phys., 25(6), 3737-3752, http://doi.org/10.5194/acp-25-3737-2025, 2025.

Kulmala, M., Cai, R., Stolzenburg, D., Zhou, Y., Dada, L., Guo, Y., Yan, C., Petäjä, T., Jiang, J., Kerminen, V. M: The contribution of new particle formation and subsequent growth to haze formation, Environ. Sci.: Atmos., 2: 352–361, https://doi.org/10.1039/D1EA00096A, 2022.

Kulmala, M., Kokkonen, T., Ezhova, E., Baklanov, A., Mahura, A., Mammarella, I., Bäck, J., Lappalainen, H. K., Tyuryakov, S., Kerminen, V., Zilitinkevich, S., Petäjä, T. Aerosols, Clusters, Greenhouse Gases, Trace Gases and Boundary-Layer Dynamics: on Feedbacks and Interactions. Boundary Layer Meteorol., 186(3), 475-503, http://doi.org/10.1007/s10546-022-00769-8, 2023.

Lata, N. N., Cheng, Z. Z., Dexheimer, D., Zhang, D. M., Mei, F., China, S. Vertical Gradient of Size-Resolved Aerosol Compositions over the Arctic Reveals Cloud Processed Aerosol in-Cloud and above Cloud. Environ. Sci. Technol., 57(14): 5821-5830, https://doi.org/10.1021/acs.est.2c09498, 2023.

Li, X. L., Ma, Y. J., Wang, Y. F., Wei, W., Zhang, Y. H., Liu, N. W., Hong, Y. Vertical Distribution of Particulate Matter and its Relationship with Planetary Boundary Layer Structure in Shenyang, Northeast China. Aerosol Air Qual. Res., 19(11), 2464-2476, https://doi.org/10.4209/aaqr.2019.06.0311, 2019.

Li, Y. Study on Vertical Atmospheric Observation Based on Tethered Balloon Platform in Wuqing Aera[D], Chinese Research Academy of Environmental Sciences, Beijing. https://link.cnki.net/doi/10.27510/d.cnki.gzhky.2019.000016, 2019.

Liu, B., Wu, C., Ma, N., Chen, Q., Li, Y. W., Ye, J. H., Martin, S. T., Li, Y. J. Vertical profiling of fine particulate matter and black carbon by using unmanned aerial vehicle in Macau, China. Sci. Total Environ., 709, 136109, http://doi.org/10.1016/j.scitotenv.2019.136109, 2020.

Lu, Y., Zhu, B., Huang, Y., Shi, S. S., Wang, H. L., An, J. L., Yu, X. N. Vertical distributions of black carbon aerosols over rural areas of the Yangtze River Delta in winter. Sci. Total Environ., 661, 1-9, http://doi.org/10.1016/j.scitotenv.2019.01.170, 2019.

Mazzola, M., Busetto, M., Ferrero, L., Viola, A. P., Cappelletti, D. AGAP: an atmospheric gondola for aerosol profiling. Rendiconti Lincei-Scienze Fisiche E Naturali, 27(Suppl 1),

105-113, http://doi.org/10.1007/s12210-016-0514-x, 2016.

Moorthy, K. K., Babu, S. S., Sunilkumar, S. V., Gupta, P. K., Gera, B. S. Altitude profiles of aerosol BC, derived from aircraft measurements over an inland urban location in India. Geophys. Res. Lett., 31(22), http://doi.org/10.1029/2004GL021336, 2004.

Morgan, W. T., Allan, J. D., Bower, K. N., Capes, G., Crosier, J., Williams, P. I., Coe, H. Vertical distribution of sub-micron aerosol chemical composition from North-Western Europe and the North-East Atlantic. Atmos. Chem. Phys., 9, 5389–5401, https://doi.org/10.5194/acp-9-5389-2009, 2009.

Olson, M. R., Victiria, G. M., Robinson, M. A., Rooy, P. V., Dietenberger, M. A., Bergin, M., Schauer, J. J. Investigation of black and brown carbon multiple-wavelength-dependent light absorption from biomass and fossil fuel combustion source emissions. J. Geophys. Res.-Atmos., 120(13): 6682-6697, https://doi.org/10.1002/2014JD022970, 2015.

Panicker, A. S., Pandithurai, G., Safai, P. D., Dipu, S., Prabha, T. V., Konwar, M. Observations of black carbon induced semi direct effect over Northeast India. Atmos. Environ., 98, 685-692, http://doi.org/10.1016/j.atmosenv.2014.09.034, 2014.

Petaja, T., Jarvi, L., Kerminen, V. M., Ding, A. J., Sun, J. N., Nie, W., Kujansuu, J., Virkkula, A., Yang, X. Q., Fu, C. B., Zilitinkevich, S., Kulmala, M. Enhanced air pollution via aerosol-boundary layer feedback in China. Sci. Rep., 6, 18998, http://doi.org/10.1038/srep18998, 2016.

Qi, S. F., Zhao, S. P., Yu, Y., Kang, S. C. Optical properties of carbonaceous aerosols and source impacts in the Lanzhou valley: In-situ observations by means of topographical relief. Urban Clim., 59, 102302, http://doi.org/10.1016/j.uclim.2025.102302, 2025.

Ramanathan, V., Carmichael, G. Global and regional climate changes due to black carbon. Nat. Geosci., 1(4), 221-227, http://doi.org/10.1038/ngeo156, 2008.

Ran, L., Deng, Z. Z., Xu, X. B., Yan, P., Lin, W. L., Wang, Y., Tian, P., Wang, P. C., Pan, W. L., Lu, D. R. Vertical profiles of black carbon measured by a micro-aethalometer in summer in the North China Plain. Atmos. Chem. and Phys., 16(16), 10441-10454, http://doi.org/10.5194/acp-16-10441-2016, 2016.

Samad, A., Vogt, U., Panta, A., Uprety, D. Vertical distribution of particulate matter, black carbon and ultra-fine particles in Stuttgart, Germany. Atmos. Pollut. Res., 11(8), 1441-

1450, http://doi.org/10.1016/j.apr.2020.05.017, 2020.

Samset, B. H., Myhre, G. Vertical dependence of black carbon, sulphate and biomass burning aerosol radiative forcing. Geophys. Res. Lett., 38, 5, http://doi.org/10.1029/2011GL049697, 2011.

Schwarz, J. P., Weinzierl, B., Samset, B. H., Dollner, M., Heimerl, K., Markovic, M. Z., Perring, A. E., Ziemba, L. Aircraft measurements of black carbon vertical profiles show upper tropospheric variability and stability. Geophys. Res. Lett., 44(2), 1132-1140, http://doi.org/10.1002/2016GL071241, 2017.

Seibert, P., Beyrich, F., Gryning, S. E., Joffre, S., Rasmussen, A., Tercier, P. Review and intercomparison of operational methods for the determination of the mixing height. Atmos. Environ., 34(7), 1001-1027, http://doi.org/10.1016/S1352-2310(99)00349-0, 2000.

Seidel, D. J., Ao, C. O., Li, K. Estimating climatological planetary boundary layer heights from radiosonde observations: Comparison of methods and uncertainty analysis. J. Geophys. Res.-Atmos., 115(D16), D16113, http://doi.org/10.1029/2009JD013680, 2010.

Shi, S. S., Zhu, B., Lu, W., Yan, S. Q., Fang, C. W., Liu, X. H., Liu, D. Y., Liu, C. Estimation of radiative forcing and heating rate based on vertical observation of black carbon in Nanjing, China. Sci. Total Environ., 756, 11, http://doi.org/10.1016/j.scitotenv.2020.144135, 2021.

Shi, Y., Hu, F., Xiao, Z. S., Fan, G. Q., Zhang, Z. Comparison of four different types of planetary boundary layer heights during a haze episode in Beijing. Sci. Total Environ., 711, 134928, http://doi.org/10.1016/j.scitotenv.2019.134928, 2020.

Sun, X. Y., Zhou, Y., Zhao, T. L., Fu, W. K., Wang, Z., Shi, C. N., Zhang, H., Zhang, Y. Q., Yang, Q. J., Shu, Z. Z. Vertical distribution of aerosols and association with atmospheric boundary layer structures during regional aerosol transport over central China. Environ. Pollut., 362, 124967, https://doi.org/10.1016/j.envpol.2024.124967, 2024.

Wang, D. F., Huo, J. T., Duan, Y. S., Zhang, K., Ding, A. J., Fu, Q. Y., Luo, J. H., Fei, D. N., Xiu, G. L., Huang, K. Vertical distribution and transport of air pollutants during a regional haze event in eastern China: A tethered mega-balloon observation study. Atmos. Environ., 246, 118039, http://doi.org/10.1016/j.atmosenv.2020.118039, 2021a.

Wang, H. C., Wang, H. L., Lu, X., Lu, K. D., Zhang, L., Tham, Y. J., Shi, Z. B., Aikin, K., Fan, S. J., Brown, S. S., Zhang, Y. H. Increased night-time oxidation over China despite widespread decrease across the globe. Nat. Geosci., 16: 217-223, https://doi.org/10.1038/s41561-022-01122-x, 2023.

Wang, H. L., Liu, A. K., Zhen, Z. X., Yin, Y., Li, B., Li, Y. Y., Chen, K., Xu, J. P. Vertical Structures of Meteorological Elements and Black Carbon at Mt. Tianshan Using an Unmanned Aerial Vehicle System. Remote Sens., 13(7), 1267, http://doi.org/10.3390/rs13071267, 2021b.

Wang, M., Xu, B. Q., Yang, S., Gao, J., Zhang, T. H., He, Z. Q., Kobal, M., Hansen, A. D. A. Black carbon profiles from tethered balloon flights over the southeastern Tibetan Plateau. Chin. Sci. Bull., 64(27): 2949-2958, https://doi.org/10.1360/TB-2019-0101, 2019.

Wang, Y. Q. MeteoInfo: GIS software for meteorological data visualization and analysis. Meteorol. Appl., 21(2), 360-368. http://doi.org/10.1002/met.1345, 2014.

Wang, Z. L., Huang, X., Ding, A. J. Dome effect of black carbon and its key influencing factors: a one-dimensional modelling study. Atmos. Chem. Phys., 18(4), 2821-2834, http://doi.org/10.5194/acp-18-2821-2018, 2018a.

Wang, Q. Q., Sun, Y. L., Xu, W. Q., Du, W., Zhou, L. B., Tang, G. Q., Chen, C., Cheng, X. L., Zhao, X. J., Ji, D. S., Han, T. T., Wang, Z., Li, J., Wang, Z. F. Vertically resolved characteristics of air pollution during two severe winter haze episodes in urban Beijing, China. Atmos. Chem. Phys., 18(4), 2495-2509, http://doi.org/10.5194/acp-18-2495-2018, 2018b.

Wendisch, M., Hellmuth, O., Ansmann, A., Heintzenberg, J., Engelmann, R., Althausen, D., Eichler, H., Müller, D., Hu, M., Zhang, Y. Radiative and dynamic effects of absorbing aerosol particles over the Pearl River Delta, China. Atmos. Environ., 42(25), 6405-6416, http://doi.org/10.1016/j.atmosenv.2008.02.033, 2008.

Wu, C., Liu, B., Wu, D., Yang, H. L., Mao, X., Tan, J., Liang, Y., Sun, J. Y., Xia, R., Sun, J. R., He, G. W., Li, M., Deng, T., Zhou, Z., Li, Y. J. Vertical profiling of black carbon and ozone using a multicopter unmanned aerial vehicle (UAV) in urban Shenzhen of South China. Sci. Total Environ., 801, http://doi.org/10.1016/j.scitotenv.2021.149689, 2021.

Wu, C. and Yu, J. Z.: Determination of primary combustion source organic carbon-to-

elemental carbon (OC / EC) ratio using ambient OC and EC measurements: secondary OC-EC correlation minimization method. Atmos. Chem. Phys., 16, 5453-5465, doi:10.5194/acp-16-5453-2016, 2016.

Xie, C. H., Xu, W. Q., Wang, J. F., Wang, Q. Q., Liu, D. T., Tang, G. Q., Chen, P., Du, W., Zhao, J., Zhang, Y. J., Zhou, W., Han, T. T., Bian, Q. Y., Li, J., Fu, P. Q., Wang, Z. F., Ge, X. L., Allan, J., Coe, H., Sun, Y. L. Vertical characterization of aerosol optical properties and brown carbon in winter in urban Beijing, China. Atmos. Chem. Phys., 19(1), 165-179, http://doi.org/10.5194/acp-19-165-2019, 2019.

Yang, X. Y., Ji, D. S., Li, J. W., He, J., Gong, C. S., Xu, X. J., Wang, Z., Liu, Y., Bi, F., Zhang, Z. Z., Chen, Y. B. Impacts of springtime biomass burning in Southeast Asia on atmospheric carbonaceous components over the Beibu Gulf in China: Insights from aircraft observations. Sci. Total Environ., 857, 10, http://doi.org/10.1016/j.scitotenv.2022.159232, 2023.

Yang, Y., Zhao, D. L., Huang, Y., Tian, P., Liu, D. T., Huang, M. Y., He, H., Ding, D. P., Li, Y. Y., Zhao, C. Effects of black carbon aerosol on air quality and vertical meteorological factors in early summer in Beijing. Sci. Total Environ., 847, 10, http://doi.org/10.1016/j.scitotenv.2022.157529, 2022.

Zarzycki, C. M., Bond, T. C. How much can the vertical distribution of black carbon affect its global direct radiative forcing? Geophys. Res. Lett., 37(20), http://doi.org/10.1029/2010GL044555, 2010.

Zawadzka, O., Posyniak, M., Nelken, K., Markuszewski, P., Chilinski, M. T., Czyzewska, D., Lisok, J., Markowicz, K. M. Study of the vertical variability of aerosol properties based on cable cars in-situ measurements. Atmos. Pollut. Res., 8(5), 968-978, http://doi.org/10.1016/j.apr.2017.03.009, 2017.

Zhang, H. S., Zhang, X. Y., Li, Q. H., Cai, X. H., Fan, S. J., Song, Y., Hu, F., Che, H. Z., Quan, J. N., Kang, L., Zhu, T. Research progress on estimation of atmospheric boundary layer height. Acta Meteorol. Sin., 78(3), 522-536, http://doi.org/10.11676/qxxb2020.044, 2020.

Zhang, Y. Z., Forrister, H., Liu, J. M., Dibb, J., Anderson, B., Schwarz, J. P., Perring, A. E., Jimenez, J. L., Campuzano-Jost, P., Wang, Y. H., Nenes, A., Weber, R. J. Top-of-

atmosphere radiative forcing affected by brown carbon in the upper troposphere. Nat. Geosci., 10(7), 486, http://doi.org/10.1038/NGEO2960, 2017.

Zhao, D. D., Xin, J. Y., Gong, C. S., Quan, J. N., Wang, Y. S., Tang, G. Q., Ma, Y. X., Dai, L. D., Wu, X. Y., Liu, G. J., Ma, Y. J. The impact threshold of the aerosol radiative forcing on the boundary layer structure in the pollution region. Atmos. Chem. Phys., 21(7), 5739-5753, http://doi.org/10.5194/acp-21-5739-2021, 2021.

Zhao, S. P., He, J. J., Dong, L. X., Qi, S. F., Yin, D. Y., Chen, J. B., Yu, Y. Contrasting Vertical Circulation between Severe and Light Air Pollution inside a Deep Basin Results from the Collaborative Experiment of 3D Boundary-Layer Meteorology and Pollution at the Sichuan Basin (BLMP-SCB). Bull. Am. Meteorol. Soc., 104(2), E411-E434, http://doi.org/10.1175/BAMS-D-22-0150.1, 2023a.

Zhao, S. P., Qi, S. F., Yu, Y., Kang, S. C., Dong, L. X, Chen, J. B., Yin, D. Y. Measurement report: Contrasting elevation-dependent light absorption by black and brown carbon: lessons from in situ measurements from the highly polluted Sichuan Basin to the pristine Tibetan Plateau. Atmos. Chem. Phys., 22(22), 14693-14708, http://doi.org/10.5194/acp-22-14693-2022, 2022.

Zhao, S. P., Yu, Y., Yin, D. Y., Yu, Z. S., Dong, L. X., Mao, Z. L., He, J. J., Yang, J. C., Li, P., Qin, D. H. Concentrations, optical and radiative properties of carbonaceous aerosols over urban Lanzhou, a typical valley city: Results from in-situ observations and numerical model. Atmos. Environ., 213, 470-484, http://doi.org/10.1016/j.atmosenv.2019.06.046, 2019.

Zhao, S. P., Yu, Y., He, J. J., Dong, L. X., Qi, S. F. A New Physical Mechanism of Rainfall Facilitation to New Particle Formation. Geophys. Res. Lett., 51(1), e2023GL106842, https://doi.org/10.1029/2023GL106842, 2023b.